Insights into Subduction Zone Sulfur Recycling from Isotopic Analysis of Eclogite-Hosted Sulfides

*K.A. Evans[1], A.G. Tomkins[2], J. Cliff [3] and M.L. Fiorentini

1. School of Applied Geology, Curtin University, GPO Box 1987, Perth, WA6845, Australia
2. School of Geosciences, Monash University, Melbourne, Victoria 3800, Australia
3. Centre for Microscopy, Characterisation and Analysis, University of Western Australia, Crawley, Perth, WA6009, Australia
4. Centre for Exploration Targeting, ARC Centre of Excellence for Core to Crust Fluid Systems (CCFS), The University of Western Australia, 35 Stirling Highway, Crawley 6009, Western Australia

*Corresponding Author Details:
Katy Evans
Email: k.evans@curtin.edu.au
Phone: +61 8 92664682
Fax: +61 8 92663153

Keywords: Sulfur, sulfur cycle, subduction, arc, porphyry copper

Abstract

Subduction of sulfur in ocean crust makes a significant but poorly understood contribution to the global sulfur cycle. Part of the uncertainty arises from a lack of knowledge about the metamorphic changes that affect subducted sulfur-bearing minerals, and the ultimate source of sulfur that is subducted to depth. Sulfur $\delta^{34}S$ varies both as a function of the original sulfur source, and as a consequence of processes subsequent to sulfide crystallization such as devolatilisation, redox reactions, and fluid loss. To investigate sulfur liberation during subduction, secondary ion mass spectroscopy (SIMS) was used to measure $\delta^{34}S$ in grains of pyrite, chalcopyrite and pyrrhotite in eclogites from the Zermatt-Saas zone in the Western Alps, and the Pouébo terrain of New Caledonia. Trace element mapping on selected sulphide grains was also performed.

Sulfides in these rocks are generally associated with greenschist retrogression assemblages, but also occur as inclusions in garnet, associated with glaucophane and omphacite, and as polysulfide grains with typical magmatic combinations of minerals. $\delta^{34}S$ varies significantly within individual pyrite grains, with striking correlations, in some cases, between Co zoning and changes in $\delta^{34}S_{VCDT}$. $\delta^{34}S_{VCDT}$ is, in many cases, greater than 13‰, consistent with derivation from seawater-derived sulfate. The dataset suggests that sulfur isotopes in pyrite experienced little or no post-crystallisation re-equilibration, that pyrite grew under open system conditions with heterogeneous fluid flow on a thin section scale, and that sulfide growth involved sulfur addition. Prograde subduction processes most likely involved sulfur loss. Sulfide growth occurred in some samples at the very earliest stages of exhumation.

Therefore these sulfides provide useful information on the fluids present in slabs at great depths.

(Abstract = 270 words).

1. Introduction

Approximately 2.4 x 10^{12} moles of sulfur are subducted every year (Evans, 2012), which is an order of magnitude higher than the 1.6 - 3.2 x 10^{11} moles of sulfur released from arc volcanoes every year (Hilton et al., 2002). The combination of the eight electron difference between sulfate and sulfide, and the large subduction-related sulfur flux suggests that the global sulfur cycle may form a major component of the redox cycle that links the biosphere and the interior of the Earth (Canfield, 2004; Canfield et al., 2007).

Sulfur is also intimately associated with the formation of many important ore deposit types. Sulfide minerals are the major hosts of most metals of economic significance (e.g., Cu, Pb, Zn, Ni, Co, Mo, PGE, Au, Ag, Sb, Bi), some elements (e.g. Au, Ag, Cu) are transported to ore-forming locations by S-bearing ligands (Benning and Seward, 1996; Jego et al., 2010; Pokrovski et al., 2009), and exsolution of immiscible sulfide liquids in magmas promotes concentration of metals of economic and environmental interest (Mungall et al., 2006; Wallace and Edmonds, 2011). It is, therefore, hardly surprising that studies of temporal variation in ore deposit style have recognised that changes in sulfur availability and speciation are a major control on global metallogeny (Barley et al., 1998; Evans et al., 2012; Evans and Tomkins, 2011; Farquhar et al., 2010; Leach et al., 2010; Tomkins, 2013).

Despite the undoubted importance of sulfur cycling, parts of the global sulfur cycle are poorly understood. Some sulfur is recycled from oceanic crust to magmatic arcs. The S content of arc basalts is higher than that of mid ocean ridge basalt (MORB) (Wallace and Edmonds, 2011) and $\delta^{34}S$ of sulfide and sulfate minerals in subduction zone-related porphyry copper deposits, which sample supra-arc crust is elevated over magmatic values, consistent with a contribution from seawater-derived sulfur (Marini et al., 2011). These data suggest that sulfur is transported into porphyry deposits via fluids that are released from the slab and propagate upwards through the mantle (Kelley and Cottrell, 2009; Richards, 2011). This inference is supported by sulfur isotope data from arc and back arc magmatic and gaseous products with elevated $\delta^{34}S$, consistent with recycling of modern seawater sulfate, which has a $\delta^{34}S$ of around 20‰ (Marini et al., 2011; Ueda and Sakai, 1984; Woodhead et al., 1987). Some sulfate is released in fore-arc environments; observations of fluids released from the Mariana trench suggest that sulfate is released at shallow depths from sediments and altered basalt in the subducting plate into aqueous fluids that migrate up the subduction interface (Mottl et al., 2004). Some sulfur is also transported into the mantle; sulfides are common inclusions in eclogitic diamonds found in mantle xenoliths (Aulbach et al., 2010; Aulbach et al., 2012). The notion of deep recycling over at least the last 2.45 Ga is supported by mass independent sulfur fractionation signatures in sulfide inclusions in eclogitic diamonds (Thomassot et al., 2009), and in 20 Ma basaltic lavas thought to sample ancient recycled oceanic crust (Cabral et al., 2013).

Processes on the input side of the sulfur subduction cycle are less well understood. Surprisingly little is known about the reactions that release or retain sulfur within the

98 subducting slab, or the nature and relative importance of mechanisms that release
99 sulfur into the sub-arc environment.
100
101 Sulfides are common in blueschists and eclogites, although only a small fraction of
102 papers describe sulfur-bearing phases in detail (Brown, 2007; Dale et al., 2009; Itaya
103 et al., 1985; Reinecke, 1998; Spandler et al., 2004). Sulfide textures can be
104 ambiguous, so that it is difficult to distinguish, for example, between pre-subduction
105 hydrothermal, and retrogressive pyrite. However, a combination of careful textural
106 and trace element analysis with sulfur isotope measurements may provide a means to
107 distinguish between the different sulfur sources and to recognise processes that
108 modify sulfur distribution and speciation. Over the last 100 Ma, magmatic sulfides
109 have entered subduction zones with a $\delta^{34}S$ value of around 0‰ (Ohmoto and Rye,
110 1979), seawater-derived sulfates with much higher $\delta^{34}S$ values, around 20‰ (Alt,
111 2003; Canfield, 2004), and sulfides related to sea-floor hydrothermal alteration cover
112 a range of $\delta^{34}S$ values, between -10‰ and 10‰ (Alt, 2003; Alt et al., 2007).
113 Bacterial sulfate reduction (BSR) imparts a wider range of $\delta^{34}S$ with fractionation
114 values of up to 50‰ (Canfield, 2001). Metamorphic loss of sulfur-bearing volatiles,
115 such as H_2S, changes the sulfur isotope value of the residue. These changes can be
116 estimated, given information on fractionation factors between solid and fluid-hosted
117 phases, and the extent to which the fluid – rock system operates as open or closed
118 system (e.g. Ohmoto and Rye, 1979). It may, therefore, be possible to use the sulfur
119 isotope composition of sulfides in subducted and exhumed rocks to constrain the
120 sources of sulfur and the processes experienced by these sulfides during subduction.
121

In this work, we present the results of high spatial resolution sulfur isotope, trace element, and textural analyses for sulfides hosted by blueschists, eclogites and retrogressed eclogites. The data are used to derive preliminary constraints on the subduction-related component of the sulfur cycle.

2. Geological Setting

Samples for this study were taken from three well known blueschist/ecologite localities: Pfülwe pass and Lago di Cignana in the Zermaat-Saas zone in the European Alps (Rubatto et al., 1998), and the Pouébo eclogite melange of New Caledonia (Aitchison et al., 1995). These localities were chosen because they are well studied and characterised, and because they provide examples of different geothermal gradients and subduction environments. Details of these localities are summarised briefly below.

2.1 Zermatt-Saas Zone

The Zermatt-Saas zone in the Penninic domain of the Western Alps provides spectacular km-scale ophiolites, which have been interpreted as Tethyan oceanic lithosphere formed in the late Jurassic (Rubatto et al., 1998) although more recent work suggests that the ultramafic units may, instead, be continental mantle lithosphere associated with the ocean-continent transition (Beltrando et al., 2010). The Zermatt-Saas zone has been proposed to be a continuous slice of lithosphere (Angiboust et al., 2009), based on relatively homogeneous pressures and temperatures, of around 2 GPa and 540 – 600ºC, across the block, although this interpretation is not universally held (Martin et al., 2008). The lithosphere represented by the Zermaat Saas zone was subducted and exhumed to form part of a nappe stack between 50 and 40

147 Ma(Barnicoat and Fry, 1987; Bocquet et al., 1974; Rubatto et al., 1998). The
148 ophiolite contains serpentinites (Li et al., 2004), gabbros, metabasalts, hydrothermally
149 altered mafic rocks (Martin et al., 2008) and Jurassic metasediments (Reinecke, 1991;
150 Rubatto et al., 1998).
151
152 *2.1.1 Lago di Cignana*
153 Lago di Cignana provides undisputed evidence of subducted oceanic crust that has
154 reached ultra-high pressure metamorphic (UHPM) conditions (Frezzotti et al., 2011;
155 Reinecke, 1991; Reinecke, 1998). Coesite-bearing rocks at Cignana occur within an
156 area of around 2 km^2, which is bounded by masses of serpentinised peridotites, and
157 comprise a sequence of relict coesite-glaucophane eclogites and retrogressed
158 greenschists, plus metasediments that overlie the eclogites. The fresh eclogites consist
159 of garnet + omphacite + phengite + glaucophane ± rutile. Overprinting blueschist and
160 greenschist retrogressive assemblages are common.
161
162 A Mn-rich layer lies at the base of the metasediments (Reinecke, 1991). This layer is
163 overlain by interlayered garnet + phengite + quartz schists, phengite-bearing
164 quartzites, garnet + phengite mica schists, and dolomite–bearing calc-schists
165 (Reinecke, 1998). Inclusions of chalcopyrite and pyrite have been recorded in
166 sediment-hosted garnets at Cignana (Reinecke, 1998).
167
168 *2.1.2 Pfülwe*
169 Pfülwe pass lies about 10 km east of Zermatt (Fig. 1a). Rocks in the vicinity of the
170 pass include metagabbros of the Allalin Gabbro, and eclogite metabasalts, some of
171 which locally preserve pillow lava structures (Barnicoat and Fry, 1987). Samples

172 used in this study were collected from the basaltic units. Zircon dates from the
173 gabbro adjacent to the basalts gives a Jurassic age of around 164 Ma (Rubatto et al.,
174 1998). Peak metamorphic pressures and temperatures for the Pfülwe area were
175 estimated to be >2 GPa and 550 – 600ºC (Barnicoat and Fry, 1987); it has been
176 suggested that peak pressures for the Allalin gabbro were as high as 3.5 GPa
177 (Barnicoat, 1985). Some of the basalts are partially retrogressed, but most preserve
178 eclogitic assemblages with minor evidence of modification during exhumation.
179 Minerals present are omphacite + garnet + paragonite ± glaucophane ± quartz ±
180 epidote ± chloritoid ± talc (Widmer and Thompson, 2001). High-pressure vein
181 assemblages in the area include quartz + glaucophane + ankerite, quartz + omphacite,
182 and omphacite veins. Dale et al. (2009) provide a detailed description of sulfide
183 mineral assemblages in rocks of the Allalin gabbro. Relatively unaltered gabbro
184 contains pyrrhotite, pentlandite and chalcopyrite, which are inferred to have had an
185 igneous origin. More altered gabbros, and the basalts, contain large pyrite grains,
186 which are attributed to a metamorphic-hydrothermal origin. Further evidence for pre-
187 metamorphic sulfides in these rocks is provided by Barnicoat and Fry (1987) note that
188 chalcopyrite is distributed throughout the basaltic rocks in this area, and in pre-
189 metamorphic veins.
190
191 ***2.2 Pouébo Ecologite Melange, New Caledonia***
192 Blueschists and eclogites crop out in the north-east of New Caledonia. These high
193 pressure, low temperature rocks are inferred to have formed during subduction of
194 oceanic crust in the Eocene (Black, 1977; Spandler et al., 2005). The region of
195 interest for this study are the highest pressure rocks, which lie at the north-eastern
196 corner of the island (Fig. 1b), and have been named the Pouébo terrain(Carson et al.,

197 1999; Clarke et al., 1997; Cluzel et al., 1995; Fitzherbert et al., 2003), the Pouébo
198 eclogitic melange (Spandler and Hermann, 2006), or the omphacite zone (Itaya et al.,
199 1985). These eclogites and transitional eclogites are mostly mafic, with subordinate
200 ultramafic and pelitic lithologies. The protoliths to the mafic rocks are likely to have
201 been back-arc basalts and gabbros (Spandler et al., 2004), some of which were
202 hydrothermally altered prior to subduction (Bell and Brothers, 1985; Itaya et al.,
203 1985). Peak pressures and temperatures are thought to be around 1.9 GPa and 600ºC
204 (Carson et al., 1999), although Fitzherbert et al. (2003) record slightly lower
205 pressures, 1.4 to 1.6 GPa.
206
207 Prograde minerals in mafic eclogites include garnet, omphacite and rutile; most of the
208 apparent ecologites are transitional eclogites, containing garnet, barroisitic amphibole
209 and rutile. Retrogression is common and involves growth of phengite and albite.
210 Sulfide assemblages were reviewed by Briggs et al. (1977), Itaya et al. (1985) and
211 Brown (2007). These authors reported that the majority of samples contain trace
212 amounts of pyrite in the matrix; pyrite co-exists with pyrrhotite in the upper blueschist
213 facies samples, whereas the eclogites contain Ni-bearing pyrrhotite-chalcopyrite
214 inclusions in garnet. Chalcopyrite is also observed in the matrix of the rock, but
215 polymineralic sulfides held in garnet inclusions suggest that the Cu-bearing sulfide at
216 peak metamorphic conditions was an *iss* (intermediate solid solution) with a
217 composition close to that of cubanite, $CuFe_2S_3$ (Itaya et al., 1985). Fe+Ni/S ratios of
218 pyrrhotite in the matrix are consistent with chemical re-equilibration at around 300ºC,
219 (Itaya et al., 1985), which suggests that matrix sulfides have experienced open system
220 retrogression to a greater extent than those hosted by garnet inclusions.
221

3. Methods

Samples were collected from the localities shown in Fig. 1. Thin sections were cut and polished without using water to allow retention of soluble minerals such as anhydrite. Samples for sulfur isotope analysis were selected after preliminary petrographic analysis by reflected light microscopy and were cut from polished thin section billets. The chosen samples were mounted in epoxy with in-house pyrite standard Sonora-3. The epoxy mounts were then repolished to a quality and flatness suitable for ion microprobe analysis and coated with 30 nm of high-purity gold.

The primary pyrite standard, Sonora-3, is taken from a large (~9 kg) cube of pyrite. Preliminary assessment of heterogeneity by SIMS on the IMS 1280 at the CMCA established that the lengthscale of heterogeneity within the sample was less than a cm, so 10 pieces of a sub-sample pyrite cube of about 1cm side length were analysed by laser fluorination at McGill University. This detailed subsampling analysis revealed variation in $\delta^{34}S$ along one axis of the cube, so the cube was split into three sections perpendicular to the axis along which variation was noted. The three replicates analysed from the chosen section, designated as Sonora-3, returned a value for $\delta^{34}S$ of 1.61 ± 0.08‰ (standard deviation of the mean) relative to VCDT (Valley Canyon Diablo Troilite). All $\delta^{34}S$ values reported here, for both standards and unknowns, are relative to VCDT. Correction factors for chalcopyrite and pyrrhotite to compensate for instrumental mass fractionation (IMF) were calculated by a combination of multiple analyses of chalcopyrite and pyrrhotite on the SIMS IMS 1280 at the CMCA and laser fluorination measurements of chalcopyrite (n = 5) and pyrrhotite (n=1) standard subsamples at McGill University. This work established that

$IMF_{chalcopyrite} = IMF_{pyrite} + 0‰$ (±0.02‰, $1SD_{mean}$),

and

$IMF_{pyrrhotite} = IMF_{pyrite} + 4.47‰$ ($\pm$ 0.03‰, 1 SD_{mean}, n=36).

The uncertainties on the relative IMF values are calculated from the standard deviation of the mean difference between the pairs of IMF values. The relative IMF approach was taken because, while the absolute instrumental IMF changes daily, the relative IMF between chalcopyrite and pyrite is relatively constant, justifying the use of the standard deviation of the mean in the error propagation calculations. Unless stated otherwise, external uncertainties of multiple analyses treated below are stated as 1 SD.

Major element concentrations for pyrite are very similar for the unknowns and the standards – variations in minor elements such as Co are of the order of less than a few tenths of a wt percent and are not expected to affect the IMF. Similarly, chalcopyrite compositions in the analysed samples are similar in terms of the major elements (Cu, Fe and S) to that used to test the IMF for chalcopyrite, so further correction for matrix effects is not required.

Ion microprobe analysis of sulfur isotopes was undertaken on the Cameca IMS 1280 instrument located at the Centre for Microscopy, Characterisation and Analysis at the University of Western Australia. In all cases nuclear magnetic resonance (NMR) regulation was used, an electron gun was used for charge compensation and ^{32}S, ^{33}S, and ^{34}S were measured using Faraday cup detectors. Two types of analyses were performed employing different spatial scales and analytical precision. For some analyses a static beam was used. For these analyses a 1 nA focused primary beam was used to presputter the analysis area for 10 seconds after which automatic secondary

272 centering and 10 × 4 second analysis cycles were performed. Pre-analysis rastering
273 was not performed. Other conditions include a 133 × magnification between sample
274 stage and the field aperture, 70 μm entrance slit, 4000 μm field aperture, 400 μm
275 contrast aperture, a 40 eV energy window with a 5 eV offset to the high energy side,
276 and 500 μm exit slits. Some analyses were performed with higher precision at the
277 expense of spatial resolution (Table 1, Supplementary Table 1g). For these analyses,
278 a 2.5 nA beam was used to sputter the surface for 60 seconds using a 30 x 30 um
279 raster. Following presputtering, the raster was reduced to 20 x 20 microns and
280 dynamic transfer was employed for automatic secondary centring and analysis
281 consisting of 30 x 4 second cycles. All other parameters were identical to the high-
282 spatial resolution analyses.
283
284 Average external precision (1 SD) for $\delta^{34}S$ analyses of the Sonora-3 standard
285 calculated from the standard deviation of drift-corrected values for the Sonora-3
286 primary standard were less than 0.05‰ for the high precision analyses (Table 1,
287 Supplementary Table 1g, n=36) and 0.28 for all other analyses of the Sonora-3
288 standard (Supplementary Tables 1a to 1f, n = 146). Sonora-3 high precision analyses
289 were made in a single 24 hour period. The other analyses were made over a period of
290 five consecutive days. All $\delta^{33}S$ analyses fell within uncertainty of the mass
291 dependent fractionation line so $\delta^{33}S$ results are not reported here. Data reduction and
292 error propagation follows that of Farquhar et al. (2013). Uncertainties were
293 propagated using standard methods that incorporated internal precision of individual
294 measurements, external precision of the calculated IMF of bracketing standard
295 analyses, uncertainty of the standard reference value, uncertainties in relative
296 instrumental mass fractionation (IMF) values between the primary pyrite standard and

297 other phases (chalcopyrite and pyrrhotite), and uncertainty associated with drift
298 correction coefficients (where applied).
299
300 Some analyses made close to the edge of grains, or next to pits where grains had been
301 plucked from the thin section, gave lower $\delta^{34}S$ than expected given other $\delta^{34}S$ values
302 within the sample. Such analyses were treated as suspect, on the grounds that
303 topographic relief within the sample can lead to artefacts in the analysis (Kita et al.,
304 2009). These analyses are not presented here.
305

306 Trace element mapping on the grains chosen for sulfur isotope analysis was
307 undertaken using the JEOL 8500F CL HyperProbe located at CSIRO
308 (Commonwealth Science and Industry Research Organisation) in Melbourne.
309 Operating conditions were 15 kV accelerating voltage, 100 nA beam current, dwell
310 time 40 ms, and pixel sizes ranging from 1-4 μm depending on the size of the area
311 mapped. Elements chosen for mapping included Co, As, Ni, Cu and Fe; of these Co
312 was found in trace quantities in all pyrite grains (Co Kα was measured on LifH), As
313 was not detected, and Fe, Cu and Ni were major components of various sulfide
314 phases. Particular attention was paid to the potential development of Fe depletion
315 haloes in silicate phases surrounding sulfides, which may indicate retrograde
316 conversion of pyrrhotite to pyrite.
317

318 **4. Results**

319 ***4.1 Petrographic analysis***

320 *4.1.1 Lago di Cignana*

321 4.1.1.1 Mafic Eclogite LC004

LC004 is a partially retrogressed mafic eclogite (N45.8791°, E7.5961°). High pressure minerals include omphacite, clinozoisite, deformed white micas, garnet, and rutile. Garnet grains are partially corroded (1-3 mm; mode ≈ 0.20) and zoned with inclusion-rich cores. There is a small amount (mode < 0.1) of pale glaucophane, present as rounded grains a few hundred microns in size. Retrogressive phases include fine-grained aggregates of actinolite and epidote, white mica, and ilmenite rims on rutile, with extensive development of fine-grained actinolite, epidote, muscovite (combined mode ≈ 0.30) that partially replace the peak metamorphic silicates along a pervasive shear fabric. A later phase of alteration is recorded by iron-stained carbonate porphyroblasts that cross cut all previous fabric elements (mode < 0.02). Quartz patches are present, which may represent dismembered veins. Sulfides are present in fractures, in the greenschist retrogressed parts of the rock and elsewhere in the matrix. Most sulfide grains are rounded (up to 1mm) pyrite, associated with pyrrhotite and chalcopyrite (common) and pentlandite (rare) e.g. Fig 2A,B. There does not appear to be any textural distinction between the different sulfide associations.

4.1.1.2 Metasediment Eclogite LC008A

LC008A is a quartz-rich metasedimentary eclogite (N45.8791°, E7.5961°). High-pressure minerals include quartz (mode ~ 0.35), garnet (mode ~ 0.25), and clinozoisite (mode ~ 0.1). Glaucophane is absent. Garnets exhibit three different textural zones. Garnet cores are rich in opaque inclusions; intermediate zones contain large (20 – 50 micron) quartz inclusions, whereas rims are inclusion-poor (Figs 2C, D). Chlorite is not observed in the matrix of the rock but occurs with sulfides in the quartz-rich inclusion zone in garnet (Figs 2C,D). Retrogressive minerals are

represented by patchy acicular aligned intergrowths of actinolite in pools of quartz, which are associated with radiating sprays of white micas (combined mode ~ 0.15) and minor albite. Sulfides are present in this rock as pyrite inclusions in the zones of garnet associated with the large quartz inclusions (mode ~ 0.01; Fig. 2E), and moderately abundant pyrite grains, up to 2mm in size, in parts of the matrix associated with greenschist minerals. There are minor small chalcopyrite (common) ± pyrrhotite (rare) inclusions (<100 μm) in garnet, and some chalcopyrite grains external to garnet. Large pyrite grains in a quartz vein associated with this sample reveal growth zoning and inclusions of older pyrite grains in the tarnish (Fig. 2F).

4.1.2 Pfülwe

4.1.2.1 Mafic Eclogite PF005

Sample PF005 (N46.0170°, E7.8427°) is a retrogressed transitional mafic ecologite. High pressure minerals include garnet (mode ~ 0.2, ~ 2 mm diameter), quartz (mode ~ 0.15), omphacite (mode ~ 0.15) and rutile. Glaucophane (mode ~ 0.15) occurs after omphacite and contains large inclusions of quartz and carbonate. Greenschist retrogression is recorded by rims of actinolite, locally intergrown with epidote, on garnet, clear rims on inclusion-rich garnets, actinolite rims on glaucophane (combined mode ~ 0.3), and ilmenite rims and intergrowths in rutile.

Pyrite occurs in the matrix (Fig. 2G,H) and as inclusions in the garnet rims, so at least some pyrite must have been present prior to exhumation beyond the garnet stability field. The included pyrites are polygranular with equant exteriors and show complex eccentric zoning patterns in the tarnish, similar to that observed in the matrix grains (e.g. Fig 2H). Pyrite inclusions in garnet in the analysed samples are connected to the

matrix by fractures within the garnet, so modification post-garnet growth is possible. Sulfide grains in the matrix are mostly polygranular, commonly associated with calcite, have 120° triple junctions at mutual grain boundaries, exhibit complex eccentric zoning in the tarnish, and have rounded external boundaries (e.g. Fig. 2G,H). The rounded external boundaries are in marked contrast to the equant grain shape of pyrite grains included in garnet. Where pyrite is adjacent to glaucophane, the actinolite rim on glaucophane is absent, consistent with costability of pyrite and glaucophane. Chalcopyrite is observed as rims on pyrite, as small grains surrounding pyrite in the matrix, and as small polysulfide grains that involve pyrite and chalcopyrite (PF005-0018).

4.1.2.2 Mafic eclogite PF008

PF008 (N46.0170°, E7.8427°) is less retrogressed than PF005, and contains aggregates of omphacite (mode ~ 0.5), with garnet (mode ~ 0.15, 3 – 5 mm) and rutile. Glaucophane occurs after the omphacite + garnet assemblage (mode ~ 0.05). Quartz inclusions occur in glaucophane. The garnet + omphacite and glaucophane-rich regions are separated by intergrowths, which are quite fine in places, of actinolite and epidote (combined mode ~ 0.1). Coarse white mica is also associated with the actinolite and epidote. Carbonate patches and porphyroblasts are also present. Actinolite is included in carbonate grains.

Pyrite is less common in this sample than in the more altered PF005, and occurs as equant grains away from garnet (Fig. 2I,J) and as polysulfide pyrite-chalcopyrite grains within the actinolite-epidote retrogressive patches, with chalcopyrite found as discontinuous rims on pyrite.

397

398 4.1.2.3 Mafic Eclogite ATPF-004

399 ATPF-004 (N46.0170°, E7.8427°) is a mafic eclogite that is dominated by a high
400 pressure assemblage of randomly oriented omphacite aggregates (mode ≈ 0.60) and
401 large (2-12 mm) subhedral garnets (mode ≈ 0.35), with minor rutile (mode ≈ 0.005).
402 These higher pressure minerals are variably overprinted by two stages of retrograde
403 mineral growth; the first is a high pressure assemblage, whereas the second is a
404 greenschist facies assemblage. The high pressure retrograde assemblage consists of
405 large glaucophane crystals (mode ≈ 0.05) that form partial coronae developed only in
406 pressure shadow regions around garnets, and coarse subhedral pyrite (up to 2 mm;
407 mode ≈ 0.005) and rare quartz ± dolomite grains that coexist with glaucophane in this
408 setting. Fine-grained intergrowths of actinolite, clinozoisite, and albite, with coarse
409 white micas form the second retrograde assemblage (mode < 0.01), which is weakly
410 and heterogeneously developed along narrow (up to 0.5 mm) spaced shear planes that
411 anastamose around grain boundaries of the earlier phases. Rare carbonate
412 porphyroblasts are associated with this second assemblage but appear to overprint it,
413 as in PF008.

414

415 Pyrite is connected to the actinolite-rich network and is coarser-grained than the
416 retrogressive silicate assemblage, but has euhedral faces against glaucophane and
417 omphacite (Figs 2K,L). In parts of the sample, pyrite is spatially restricted to the
418 glaucophane coronae and inclusions in garnet. In some cases, pyrite is separated from
419 omphacite and garnet by a thin film of quartz ± rutile.

420

421 *4.1.3 New Caledonia:Mafic Transitional Eclogites EH-033 and EH-028*

EH-033 is characterised by the peak metamorphic assemblage typical of Type I eclogites of the Pouébo Terrane of northeast New Caledonia (Carson et al., 1999). Abundant barroisitic amphibole (mode – 0.30-0.55) gives the rock a dark green colour. Idioblastic garnet crystals (1-3mm; mode ≈ 0.20) are zoned with high Mn, low Fe and Mg cores and mottled Ca zoning (not shown). Clinozoisite is variably abundant, with an average bulk modal proportion of ~ 0.30. Scanning electron microscope work indicates that omphacite comprises ~ 10% of the sample and is typically encapsulated in barroisite. Minor quartz, muscovite and biotite surround most garnets, implying that water has pervasively penetrated the sample on the retrograde path. Minor rutile occurs throughout the sample (mode ≈ 0.01).

Pyrite occurs as isolated sub-spherical grains up to 2 mm amongst the matrix, and as sparse rounded inclusions in the core regions of garnet, although most of these are connected to the exterior via fractures. Very small (< 20μm) chalcopyrite ± pyrrhotite ± pentlandite inclusions are also found in garnet in this sample. However, these grains were too small for SIMS analysis. Sample EH-028, which comes from a similar structural and metamorphic setting, contains pyrite and pyrite-chalcopyrite inclusions in the core zone of garnets, some of which are isolated from fractures connecting to the outside of the garnet. However, these inclusions were too small for SIMS analysis and matrix pyrite in EH-028 was not analysed because of weathering-related formation of iron oxyhydroxides.

4.2 Sulfur Isotope and Trace Element Mapping Results

4.2.1 Lago di Cignana

4.2.1.1 Mafic Eclogite LC004

447 $\delta^{34}S$ values in LC004 range from -11.5‰ to -5.8‰ (Table 1, Supplementary Table
448 1a), but $\delta^{34}S$ for the vast majority of samples lies between -6‰ and -8‰ (Fig. 3A,
449 4A-C). Measured $\delta^{34}S$ within single grains varies outside the analytical uncertainty
450 and indicates intra-grain heterogeneity. The two smallest grains analysed have the
451 heaviest average $\delta^{34}S$ value and the smallest standard deviation of multiple analyses
452 within a grain ($\delta^{34}S$ of -6.5 ± 0.8 (n=3, LC004-001) and -6.7 ± 0.02 (n=2, LC004-
453 003)). The two most negative $\delta^{34}S$ isotopic values (-11.5‰ and -10.1‰) both occur
454 within large grains and are outliers on a histogram of $\delta^{34}S$ values within this sample
455 (Fig. 3A).
456
457 Microprobe mapping reveals that the heterogeneity is linked to subtle zoning in the
458 trace Co content of pyrite (Figs 4A,B). Heavier sulfur isotope values occur in the Co-
459 rich region close to chalcopyrite, and lighter values in the more Co-poor, Ni-rich
460 regions far from chalcopyrite. Low Ni regions of the pyrite grain at the margins and
461 in channel-like structures within the grain (Fig. 4A) are related to parts of the pyrite
462 that are oxidised to iron oxides and are not considered further.
463
464 4.2.1.2 Metasediment Eclogite LC-008A
465 The $\delta^{34}S$ isotope values of pyrites analysed in LC008A range from -6.7‰ to 2.4‰
466 (Table 1, Supplementary Table 1b), but the bulk of the analysed pyrite grains have
467 $\delta^{34}S$ isotope values between -3‰ and +2.5‰, with a mode in $\delta^{34}S$ isotope values
468 between -1‰ and 0‰ (Fig. 3B). There is a distinct group of outliers (6 analyses)
469 with $\delta^{34}S$ values around -4‰; these negative $\delta^{34}S$ values come from the same grains
470 as those within the main group of values and there is no obvious textural or

compositional control on the location of the negative $\delta^{34}S$ values either texturally or in the trace element maps. Texturally, the pyrite grains fall into three categories:

(i) A single grain (LC008A-003b) included in garnet without visible connection to the grain exterior. Only one analysis could be made on this grain. The $\delta^{34}S$ value of 0.7‰ lies in the middle of values measured for this sample from matrix pyrite;

(ii) Grains that are included in garnet, but are connected to the main matrix of the rock (Fig. 4D). These grains include LC008A-004, and two separate grains included in a garnet and analysed as LC008A-005 points 1 to 3 and LC008A-005 points 4 to 6 (Fig 4D; Supplementary Table 1b). $\delta^{34}S$ for all of these grains also lies within the main group, with statistically indistinguishable averages and standard deviations of -0.12 ± 0.02‰ (n=5), -0.6 ± 0.6‰ (n = 3), and -0.8 ± 0.3‰ (n=3) respectively;

(iii) relatively equant matrix grains. Some matrix grains are more heterogeneous than the garnet-hosted pyrite, e.g. LC008A-006 and LC008A-003. Other matrix grains are homogeneous and similar to the garnet inclusion grains, with $\delta^{34}S$ values close to zero (e.g. Fig 4G and 4H). Four analyses on LC008A-001, for example, give an average value of -0.21 ± 0.12‰.

It is not possible to distinguish between homogeneous and heterogeneous grains using reflected light microscopy, but Co-zoning maps reveal that the trace element distribution in the two types of grain is quite different. Cobalt zoning in the isotopically heterogeneous pyrite grains is complex, indicating multiple generations of pyrite growth and resorption (Figs 4E,F). In the isotopically homogeneous grains (Figs 4G and 3H), zoning is much more subtle, or non-existent. Cobalt contents are

lower than in the metabasalt samples with Co contents less than a few tenths of a wt%.

4.2.2 Pfülwe

4.2.2.1 Mafic Eclogite PF005

$\delta^{34}S$ values in PF005 lie between 10‰ and 15‰, with a small number of outliers around 2‰ to 4‰, and some higher values, up to 16.5‰ (Table 1, Supplementary Table 1c, Fig. 3C). Most analysed pyrite grains are polygranular aggregates that lie in the matrix (Fig. 5A). One analysed aggregate is included in a garnet rim, but is connected to the matrix via altered fractures (PF005-0017).

The lowest $\delta^{34}S$ analyses are associated with distinct resorbed Co-rich cores (up to 1 wt%) within the polygranular aggregates (Fig. 5B), and the variety of observed $\delta^{34}S$ values is likely to be related to sampling of the transition between irregularly-shaped low $\delta^{34}S$, Co-rich cores and high $\delta^{34}S$, Co-poor rims.

4.2.2.2 Mafic Eclogite PF008

$\delta^{34}S$ values in PF008 are bimodal (Table 1, Supplementary Table 1d, Fig 3D), with well-defined modes at around 7‰ and 12‰. All of these grains are originally equant grains in apparently texturally late settings in the matrix, so textural setting does not distinguish the two modes. For example, grain PF008-0024 (Fig. 6A) contains analyses that fall into both groups, whereas PF008-0027 (Fig. 6B) contains analyses from the 12‰ group only and PF008-003 (Fig. 6C) contains analyses only from the 7‰ group. The grain that shows both modes (PF008-0024; Fig. 6A) is the largest grain, at several hundred microns long, whereas the single mode grains are of the

order of 100 microns in size. The polymetallic chalcopyrite-pyrite grain provides a pyrite analysis in the 7‰ group (Fig. 6D). The distribution of values is relatively homogeneous within each mode; the standard deviation of the analyses for grains that display only one of the modes is close to the standard deviation expected for a single homogeneous population.

Trace element mapping of the largest grain (PF008-024) reveals that the 12‰ group of analyses is associated with an irregularly-shaped, resorbed low Co core, whereas analyses from the 7‰ group occur in a more Co-rich rim (Fig. 6A). Cobalt contents in core and rim are low compared to the grains with $\delta^{34}S$ close to zero in sample PF005; the low Co core in grain PF008-024 has a Co content of less than 0.2 wt%, whereas the higher Co rim has a Co content generally less than 0.6 wt%.

4.2.2.3 Mafic Eclogite ATPF-004

$\delta^{34}S$ values in ATPF-004 are bimodal (Table 1, Supplementary Table 1e, Fig. 3E), like PF008, although the modes are located at 8‰ to 9‰ and 12‰ to 13‰, so that the lighter mode is a little heavier than that in PF008. Values from the 8 – 9‰ group of $\delta^{34}S$ values occur throughout the very homogenous matrix grain ATPF004-G4 (9.2 ± 0.7‰, n=5) and at the rims of grain ATPF004-G3 (Fig. 7E). Heavier values are located throughout the homogeneous matrix grain ATPF004-G2 (12.6 ± 0.4‰, n=8), at one edge of grain ATPF004-G5 (Fig. 7D), and in the centre of grain ATPF004-G3 (Fig. 7E).

$\delta^{34}S$ is related to Co concentration in grain ATPF004-G1 (Fig. 7B). The majority of the grain has a relatively low Co content, around 0.2 to 0.4 wt%, and these parts of the

546 grain have $\delta^{34}S$ in the 8 -- 9‰ group. Two high Co (0.6 – 0.7 wt% Co) bands were
547 sampled. The inner band is associated with $\delta^{34}S$ values between 7.3‰ and 7.8‰ and
548 the outer band is associated with values in the 12 to 13‰ group (Fig 7C).
549 Absolute Co contents are similar to those in mafic eclogite PF008. Cobalt zoning in
550 G1 is undisturbed at pyrite – glaucophane boundaries, but is truncated where pyrite is
551 adjacent to omphacite and garnet. Results from the Co mapping and the sulfur
552 isotope traverse across ATPF004-G1 suggest these variations are likely to be linked to
553 complex Co zoning and cyclical variation between high and low $\delta^{34}S$ values.
554
555 *4.2.3 New Caledonia*
556 4.2.3.1 Mafic Transitional Eclogite EH-033
557 The majority of SIMS $\delta^{34}S$ data for the two analysed grains of matrix pyrite from EH-
558 033 fall within a very narrow range between 4 and 6.5‰ (Table 1, Supplementary
559 Table 1f,g, Fig. 3F, G), with two analyses close to zero. The two outliers are from
560 one end of a weathered pyrite grain and are neglected in the subsequent discussion. A
561 high resolution $\delta^{34}S$ map of one of the New Caledonia grains, in which 79 analyses
562 were taken across a 600 x 600 micron pyrite grain (Fig. 8A), indicates a convex
563 concentric isotopic zoning profile (Fig. 8B), with analyses between 4.7 at the pyrite
564 margins and 5.5‰ in the core.
565
566 This zoning in $\delta^{34}S$ matches closely the growth zoning identified by Co mapping
567 (Figs. 8C and 8D). The trace element mapping reveals subtle rhythmic Co zoning in
568 the analysed grain. The periphery of the grain (Fig. 8C, D) is slightly Co-enriched,
569 and thin growth bands allow recognition of the pyrite core and progressive
570 asymmetric growth of subhedral crystal faces. The Co content is similar to that of the

571 large pyrites in mafic eclogites from Pfülwe, ATPF-004 and PF008, with values
572 ranging from 0.1 or 0.2 wt% to around 0.5 wt%. This grain is in contact with the high
573 pressure mineral assemblage (Figs 8E, F).
574
575 **5. Discussion**
576 The six samples from three locations display significant variety in the distribution of
577 sulfur isotope ratios and in the relationships between trace element content and sulfur
578 isotope values. One sample from Lago di Cignana shows dominantly negative $\delta^{34}S$
579 pyrite values (LC004), whereas the other shows values close to zero (LC008A). At
580 Pfülwe, where three samples from the same locality are examined (PF005, PF008,
581 ATPF004), we see modes of $\delta^{34}S$ centred around 5‰, 7‰ and 12‰, core $\delta^{34}S$ higher
582 than rim (PF008), rim $\delta^{34}S$ higher than core (PF005), high Co coupled with the lowest
583 $\delta^{34}S$ values in a grain (PF008) and high Co coupled with high $\delta^{34}S$ (ATPF-004). The
584 New Caledonian sample shows characteristics similar to Pfülwe
585 grains that display the 5 -- 7‰ sulfur isotope values.
586
587 To draw these apparently contrasting observations together, it is necessary to assess
588 potential contributions to the sulfide mineralogy and isotope budget made by
589 magmatic sulfides, hydrothermal alteration, prograde, and retrograde metamorphism.
590 The assessment is made on the basis of existing knowledge regarding equilibrium
591 isotope fractionation and sulfur and Co speciation, and the extent of textural and
592 isotopic re-equilibration drawn from the observations in this work.
593
594 ***5.1 Sulfur speciation in rock-buffered systems***

In rocks with pH and Eh buffered by a mafic silicate minerals plus pyrite, magnetite +/- pyrrhotite, the dominant sulfur species in solution is likely to be reduced sulfur as H_2S and HS^-, based on calculations at lower pressure and temperature in felsic rocks (Reed and Palandri, 2006), and mafic rocks (Evans, 2010; Evans et al., 2006). The solubilities of these species in the presence of pyrite is likely to be low, at 10^{-3} to 10^{-5} molal, depending on pressure, temperature, pH and redox. These solubilities are an estimate, based on experimental solubility measurements and thermodynamic calculations at pressures and temperatures different to those relevant to subduction zones (Ohmoto et al., 1994; Reed and Palandri, 2006), as there are no data or applicable thermodynamic models for pyrite solubility or aqueous sulfide/sulfate equilibria at pressures higher than 0.5 GPa.

The solubility of sulfate is much higher than that of sulfide. Newton and Manning (2005) measured the solubility of anhydrite in NaCl-H_2O solutions at temperatures up to 800ºC and pressures to 1.4 GPa. These workers found that the molality of sulfate in pure water at 800ºC and 1 GPa was at least an order of magnitude higher than the inferred reduced sulfur solubility at 0.03 molal, and that solubility increased by a factor of 200 as the mole fraction of NaCl was increased to 0.3. However, sulfate is likely to have been present only as a negligible proportion of the sulfur in the rock-buffered systems studied, so dissolution of anhydrite would produce sulfide rather than sulfate.

5.2 Fractionation of sulfur isotopes

The effect of fractionation during sulfur loss from pyrite and anhydrite was calculated at 300ºC for starting compositions of anhydrite in equilibrium with seawater sulfate

620 and pyrite derived from magmatic and hydrothermal sulfides (Fig. 9A, B). These
621 calculations are not intended to provide information on where, how, or in what
622 medium the sulfur loss occurred, but only to assess the changes associated with
623 fractionation to allow potential sources to be constrained. Closed system (Fig. 9A)
624 and open system Rayleigh (Fig. 9B) fractionation are the two end-members of the
625 fractionation process; in reality, during deformation and metamorphism, conditions
626 are likely to have cycled between the two end-members. The single chosen
627 temperature is a simplification because sulfur loss proceeded at a range of
628 temperatures up to 500 or 600ºC. The value of 300ºC was chosen because
629 fractionation factors are greater at lower temperatures so this temperature allows
630 calculation of the maximum effect of devolatilisation on sulfur isotope values.
631
632 Fractionation between reduced sulfur species and minerals, such as pyrite, H_2S and
633 pyrrhotite is relatively minor at the temperatures of interest. For example $\Delta_{pyrite\text{-}H2S}$ is
634 1.2‰ at 300ºC and 0.7‰ at 500ºC (Ohmoto and Rye, 1979). Fractionation between
635 these reduced species is therefore unlikely to have a large effect on the sulfur isotope
636 signature of sulfide minerals, and sulfide minerals are likely to reflect the isotope
637 signature of the source fluid quite closely.
638
639 Fractionation between sulfate and sulfide, on the other hand, is much stronger. $\Delta_{sulfate\text{-}}$
640 $_{sulfide}$ is around 20‰ at 300ºC and 15‰ at 500ºC (Ohmoto and Rye, 1979), so sulfate –
641 sulfide species transitions could cause large departures from the isotope signature of
642 the starting species. However, sulfate species are unlikely to be stable in solution
643 with the observed mineral buffering assemblages, so these large fractionations are not
644 expected in the systems of interest.

645

646 The S^{3-} ion might become significant at temperatures above 250ºC and below 450ºC,
647 and pressures above 0.5 GPa (Pokrovski and Dubrovinsky, 2011) so this species
648 could occur in subduction zone settings. Isotope fractionation values for S^{3-} have not
649 been measured so it is not possible to incorporate S^{3-} quantitatively into the models
650 presented here. However, sulfur isotope fractionation relates in a systematic way to
651 valence, so the average S valence of -1/3 in S_3^- suggests that $\Delta_{S3-pyrite}$ values should be
652 similar, but of opposite sign, to that of $\Delta_{H2S-pyrite}$.

653

654 ***5.3 Trace Element Controls: Cobalt***

655 Cobalt is transported in hydrothermal fluids primarily as the $CoCl_4^{2-}$ complex (Liu et
656 al., 2011); smaller amounts can be transported as $CoHS^+$, which becomes less
657 important with increasing temperatures above 200°C (Migdisov et al., 2011). Because
658 of its similarity in atomic radius and charge to Fe, Co substitutes into the crystal
659 structure of ferromagnesian silicate phases. It is also a common minor component of
660 magmatic sulfide minerals. The Co content of pyrrhotite, pentlandite and
661 chalcopyrite in unaltered Allalin gabbro, which are inferred to be of magmatic origin,
662 are 0.05 wt%, 1.62 and 0.01 wt% respectively (Dale et al., 2009). Given the minor
663 abundance of sulfides in eclogite protoliths relative to ferromagnesian silicates (e.g.
664 Dale et al., 2009), the latter are likely to be the more important source for Co in
665 hydrothermal pyrite, so Co could be sequestered into the weakly saline fluids
666 produced by slab dehydration. Cobalt solubility increases with Cl content of the fluid,
667 (Liu et al., 2011) so high Co zones in pyrite may reflect the passage of more saline
668 fluids. Subduction zone fluids released by antigorite + brucite dehydration in
669 serpentinised oceanic mantle lithosphere through 550-600°C can be highly saline

(Kendrick et al., 2011), although other workers have proposed that serpentine-derived fluids are low salinity (Aulbach et al., 2012). Regardless, it is likely that mafic- and ultramafic-derived fluids are likely to have different salinities, so Co zoning may record the passage of fluids from different sources.

5.4 Preservation of textural and isotopic information

Several observations are consistent with limited equilibration of sulfur isotopes in subducted mafic rocks by hydrothermal and metamorphic processes. Observations that support this proposal include individual pyrite grains in PF008 that are homogeneous with respect to $\delta^{34}S$ but with 6‰ variation between grains (e.g. grains PF008-027 and PF008-003) and 6‰ $\delta^{34}S$ excursions on a 20 micron scale in Pfülwe sample ATPF004 (Fig 7B). This restricted isotopic equilibrium contrasts with common 120º internal grain boundaries (e.g. Fig 5C), which suggest textural equilibrium. Pyrite tends to deform by brittle, rather than ductile, mechanisms at the temperatures of interest (McClay and Ellis, 1983). It is therefore likely that fracturing facilitates fluid-mediated dissolution-precipitation reactions on a very local scale. Fracturing followed by new pyrite growth could produce the observed 120º triple junctions, while preserving local variations in isotope composition. This fluid-mediated dissolution and reprecipitation is consistent with the observed Co zoning in pyrite grains, which indicates resorption followed by new growth (e.g., Fig. 6B). The preservation of fine-scale Co zoning in every pyrite mapped indicates that there was no metamorphic annealing. Interpretation is therefore made on the basis that sulfur isotope values record the fluids that the sulfides formed from, and that metamorphic reequilibration was minor or non-existent.

695 ***5.5 Sulfur-bearing minerals in the protolith***

696 Magmatic sulfide in oceanic basalts and gabbros occurs as pyrrhotite with
697 chalcopyrite +/- pentlandite (Miller and Cervantes, 2002; Puchelt et al., 1996). As
698 melts cool, sulphides precipitate initially as *mss* (monosulfide solid solution) and *iss*
699 (intermediate solid solution) then exsolve during cooling to form small composite
700 grains with varying proportions of the three main sulphide minerals. This primary
701 assemblage is retained in parts of the Allalin gabbro in the Pfülwe pass that have not
702 experienced significant metamorphic crystallisation (Dale et al., 2009), and is also
703 observed in sulfide assemblages in eclogitic diamonds in mantle xenoliths (Aulbach et
704 al., 2012).

705

706 The combination of pyrrhotite with chalcopyrite and minor pentlandite in LC004 (Fig.
707 4A, B) is typical of primary magmatic sulfide assemblages formed during basalt
708 crystallisation, whereas the presence of pyrite suggests sulfidation by $FeS + 1/2S_2 =$
709 FeS_2, or similar, post crystallisation. Post crystallisation modification is also
710 suggested by the isotope values, which are heavier than expected for primary
711 magmatic assemblages. Primary sulfides in mafic rocks have $\delta^{34}S$ close to 0‰, even
712 after moderate hydrothermal alteration in the ocean crust (Alt, 1995; Puchelt et al.,
713 1996), so the negative values in LC004 require some process in addition to
714 recrystallisation of magmatic sulfides. Primary sulfur may also be present in mafic
715 eclogite sample PF005, which contains low $\delta^{34}S$ cores with a Co content similar to the
716 pyrrhotite-pentlandite- chalcopyrite-pyrite grain in LC004 (Fig. 5B). The $\delta^{34}S$ value
717 of these cores could represent magmatic sulfide values (Fig. 9A,B), after minor or
718 extensive devolatilisation of H_2S. The characteristics of these composite grains in
719 LC004 are therefore consistent with derivation from Co-rich primary magmatic

720 sulphides. Further evidence for preservation of features associated with primary
721 sulfides are provided by the Cu-rich, Ni-bearing of polysulfide grains included in
722 garnet from New Caledonian transitional eclogite sample EH-033. These grains may
723 have been originally primary magmatic sulfides.
724
725 Sulfur in sediments, such as those metamorphosed to form LC008A, usually occurs as
726 pyrite formed by bacterial sulfate reduction (BSR) during diagenesis. Sulfides must
727 have been present in LC008A prior to garnet growth, as texturally equilibrated
728 sulfides occur as inclusion phases in garnet. $\delta^{34}S$ values close to zero are consistent
729 with pyrite formed from seawater via bacterial sulfate reduction in an open system
730 during sedimentation and/or diagenesis (Ohmoto and Goldhaber, 1997). The values
731 and interpretation are consistent with those of (Alirezaei and Cameron, 2001), who
732 studied metasediments in the Bamble terrain, Norway where granulite grade
733 metasediments retain signatures attributed to BSR even after conversion of pyrite to
734 pyrrhotite.
735
736 An alternative explanation for near-zero $\delta^{34}S$ values is growth of pyrite from H_2S
737 derived from a magmatic source. Adequate volumes of basalts for the latter
738 explanation are close to the metasediment outcrop where LC004 was taken, but pure
739 magmatic signatures are improbable given the BSR signature inferred for sulfides in
740 metabasalt sample LC004, so the BSR explanation is preferred. Cobalt zoning in
741 some grains in the metasedimentary LC008A (Fig. 4F) suggests a complex history of
742 growth followed by resorption and further growth, although it is not possible to assign
743 the growth and resorption to specific events.
744

745 ***5.6 Sulfur-bearing minerals associated with diagenesis/hydrothermal alteration***

746 Pyrite forms as a result of hydrothermal alteration of the ocean crust (Alt et al., 2007;
747 Walther, 1991) and involves the addition of seawater-derived sulfur (Fig. 10A).
748 Alteration may occur prior to subduction, when basalts interact with seawater during
749 on and off-ridge axis hydrothermal circulation (Alt, 2003). Additional hydrothermal
750 circulation may occur as the slab bends to enter the subduction zone (Ranero and
751 Sallares, 2004). Alteration can be partial or complete, and can affect basalts and
752 gabbros (Puchelt et al., 1996). The $\delta^{34}S$ of sulfides that form as a result of
753 hydrothermal alteration varies between -10 and +10‰ (Grinenko et al., 1975;
754 Ohmoto and Rye, 1979 1991) depending on the balance of magmatic to seawater
755 sulfur and the extent to which the system was open or closed. Hydrothermal sulfides
756 in basalt-hosted ores from the Northern Apennines, which have undergone only slight
757 metamorphism have $\delta^{34}S$ with an average of 7.9‰, although this is based on only four
758 samples (Garuti et al., 2009). The sulphide phase assemblage in these ores is pyrite-
759 chalcopyrite-sphalerite, with pyrrhotite, marcasite, covellite and other accessory
760 minerals. Sulfates, such as anhydrite, derived from seawater sulfate have fluctuated
761 around +20‰ over the last 100 Ma (Canfield, 2004).
762
763 The sulfur concentration of typical MORB is 800-1500 ppm (Jenner et al., 2010) and
764 average continental lithosphere values are no higher (Hartmann and Wedepohl, 1993;
765 Rudnick and Fountain, 1995). Sulfide modes in the samples (1-2 vol%) chosen for
766 this study are in excess of modes consistent with this value (around 0.2 vol%), so
767 addition of sulfur after igneous crystallization must have occurred.
768

769 The simplest explanation for the pyrites with $\delta^{34}S$ values around 7‰ is that the sulfur
770 in these pyrites was originally hosted by hydrothermal pyrite. The pyrites may have
771 remained relatively unaltered, or, as we suggest is more likely, the sulfur may have
772 moved, dissolved in a fluid, from one location to another during subduction zone
773 metamorphism. Pyrite with $\delta^{34}S$ values around 7‰ is not observed as inclusions in
774 garnet in the Alpine Pfülwe samples, so it is not possible to demonstrate that
775 hydrothermal pyrite grains survived from oceanic alteration to exhumation. The
776 proposed hydrothermal $\delta^{34}S$ signature is commonly observed with the heavier 12‰
777 signature in grains with complex zoning such as those in samples PF008 (Fig. 6A)
778 and ATPF-004. This supports the view that at least some of the hydrothermal sulfur
779 was remobilized during subduction and/or exhumation (sections 5.8 and 5.9).
780
781 A hydrothermal sulfur source is consistent with measured $\delta^{34}S$ values in matrix pyrite
782 in the New Caledonia sample of 4 to 6 ‰ (Fig. 8B), with a coincident decrease in Co
783 content and $\delta^{34}S$ values from core to rim, associated with fine scale rhythmic Co
784 zoning. The lack of distinct changes in Co content or truncation of Co-zoning and the
785 subtle change in $\delta^{34}S$ from core to rim in this pyrite grain are consistent with a single,
786 relatively chemically invariant, growth event. Hydrothermal sulfides are known to
787 occur in metamorphosed sulfide deposits within the New Caledonian high pressure
788 terrain (Itaya et al., 1985), but the position of the pyrite in Fig. 8 looks texturally late,
789 so it is likely that this sulfur was remobilized during metamorphism (sections 5.8 and
790 5.9).
791
792 ***5.7 Prograde Metamorphism***

There is little evidence for sulfide growth during prograde metamorphism, although the presence of typical magmatic assemblages (LC004, EH-028), pyrite inclusions in garnet (LC008A, PF005) and magmatic isotope signatures in high Co pyrite cores (PF005) suggest that sulfur is not completely lost from these rocks during prograde metamorphism (Fig. 10B). Retention of some sulfur through subduction and beyond is also consistent with the presence of pyrrhotite in eclogitic diamonds in xenoliths (e.g. Aulbach et al., 2012), and with the relatively low solubility of H_2S in fluids inferred to have been present in the subduction zone.

Prograde transformation of the polysulfide grain in LC004 to a pyrite-bearing assemblage is suggested by the negative isotope signature of the sulfides (Fig. 4B), which suggests that these grains may have incorporated lighter sulfur at some stage. The most likely source for this light sulfur is BSR (section 5.5). Prograde recrystallization in ultra-high temperature (UHT) rocks is proposed by Kawakami et al. (2006) to account for pyrrhotite-pentlandite-chalcopyrite polyphase sulfide inclusion assemblages in garnets from the Lutzo-Holm complex, Antarctica.

Most trace element and isotopic studies of subducted samples suggest that fluids in subduction zones are locally sourced and in equilibrium with their wallrocks (e.g. Scambelluri and Philippot, 2001). If this is true, fluid movement on large scales during prograde subduction zone metamorphism must be channelised, rather than pervasive and associated with extensive fluid-rock interaction. The observations and interpretations drawn from sulfide assemblages documented here are consistent with channelised fluid flow during prograde metamorphism, and if this was the case then

817 sulfur lost from the rock would have been removed from the immediate site of
818 devolatilisation by channelized flow.
819
820 ***5.8 Blueschist Retrogression***
821 Pyrite growth is associated unambiguously with blueschist retrogression in samples
822 PF005 and ATPF-004. These pyrites have Co contents of a few tenths of a weight
823 percent, which is significantly lower than Co contents of sulfides with inferred
824 magmatic precursors in mafic eclogite samples LC004 and PF005, which have Co
825 contents up to 1 wt%. A number of lines of evidence suggest that externally derived
826 fluids infiltrated the rocks at this time. For example, in PF008, truncation of the
827 sulfur and Co zoning in the largest grain analysed (Fig. 6A) are consistent with
828 periods of sulfide resorption during and after grain growth, suggesting that the fluid
829 composition cycled between pyrite-saturated and pyrite-undersaturated during
830 metamorphism and retrogression. Cyclical variations in Co content and S isotope
831 values, and periods of resorption, suggest that there was cyclical variation in the trace
832 element and sulfur isotope composition of infiltrating fluid, rather than a constant or
833 gradually evolving fluid composition for each stage of the rock's history. Fry and
834 Barnicoat (1987) also invoked fluid influx at peak pressure or the earliest stages of
835 exhumation to drive growth of glaucophane in rocks from the Pfülwe locality.
836
837 Blueschist assemblages require a source of fluid and sulfur at depths greater than 20
838 km, and, most likely, at depths greater than that of the studied rocks. Metamorphic
839 fluids are produced at the blueschist-eclogite transition, and by ultramafic rocks
840 during serpentine dehydration. These fluids could carry H_2S or S_3^- produced by pyrite
841 dissolution or at the pyrite-pyrrhotite transition, and/or dissolve sulfate as H_2S to

842 produce the observed heavy sulfur isotope signature. It is therefore possible that
843 fluids associated with blueschist retrogression sampled levels of the subducting slab.
844 Sources proposed to account for greenschist retrogression, such as passage through
845 dehydration reactions from the low temperature side (e.g. Miller and Cartwright,
846 2006), and juxtaposition during exhumation with sediments accreted in a subduction
847 melange or the accretionary wedge (Fry and Barnicoat, 1987) must also be
848 considered, but these are less likely to have provided fluids that could have infiltrated
849 the slab at the required depths. Retrograde fluids may also become available as a
850 result of decompressional exsolution of structural hydroxyl water from nominally
851 anhydrous minerals such as omphacite, and the decomposition of hydrous UHP
852 minerals (Zheng, 2009). Such fluids have the capacity to transport elements and drive
853 retrogression, however, their volume is likely to be small relative to that of the
854 devolatilisation fluids from lower grade rocks.
855
856 Although most studies of subducted samples suggest fluid flow in subduction zones is
857 channelized (section 5.7), some field evidence suggests that dehydration can induce
858 brittle cracking and veining during subduction and that the fluids migrate locally and
859 produce hydrofractures in surrounding units (Healy et al., 2009; Philippot and
860 Selverstone, 1991; Widmer and Thompson, 2001). This process could drive
861 infiltration of out-of-equilibrium fluids into the basaltic lithologies studied. For
862 example, high Ni and Cr contents of vein omphacite in Monviso gabbros (Spandler et
863 al., 2011) are consistent with infiltration of serpentinite-derived fluids. Similar
864 conclusions are drawn by Padron-Navarta et al. (2010), who infer pervasive
865 infiltration of Si-undersaturated, serpentinite-derived fluids into hydrated mantle
866 wedge chlorite harzburgites in the Betic Cordilleras. An explanation consistent with

867 the observations described here is that, although fluid flow during normal subduction
868 is channelized, more pervasive but highly variable infiltration is facilitated by changes
869 in stresses associated with a dysfunctional subduction zone. Indeed, the occurrence of
870 glaucophane in pressure fringes around garnet in ATPF-004 indicates pervasive
871 infiltration of fluid through this sample during ductile deformation under blueschist
872 conditions.
873
874 The heterogeneous distribution of pyrite, which occurs, for example with glaucophane
875 in garnet pressure shadows (ATPF-004) suggests that retrograde fluid flow was
876 heterogeneous on the thin section scale and above. Fluid:rock ratios cannot have been
877 sufficiently large that the systems were fluid-buffered with respect to sulfur, since
878 high variance metasomatic mineral assemblages, extensive recrystallization and
879 consequently homogenised sulfur isotope values are not observed.
880
881 At least two sources of sulfur are required to explain the measured sulfur isotope
882 distribution associated with blueschist retrogression sulfides. One group of
883 measurements, with $\delta^{34}S$ around 7‰, is consistent with derivation from hydrothermal
884 sulfides, either locally or external to the samples studied. If H_2S was derived locally
885 from rocks at pressures and temperatures within the pyrite stability field, then sulfide
886 growth would reflect only local redistribution of sulfur. If, however, H_2S was derived
887 from rocks deeper in the subducting slab, then sulfur could be derived from
888 conversion of pyrite (S:Fe = 2) to pyrrhotite (S:Fe ~ 1) (Barton and Toulmin, 1964a;
889 Toulmin and Barton, 1964) and/or conversion of chalcopyrite (S:metal = 1) to bornite
890 (S:metal = 0.66) (Barton and Toulmin, 1964b). More detailed studies of the
891 distribution of sulfides with relation to possible fluid pathways on different

892 lengthscales is required to resolve the local vs. external derivation question.
893 Significant H_2S is not likely to have been supplied by either exhumation-related
894 dehydration reactions or by fluids sourced from sediments, so long as the rocks
895 remain within the pyrite stability field. An alternative explanation for pyrite grains
896 with $\delta^{34}S$ around 7‰ is a mixture of magmatic and sulfate-derived sulfur from
897 separate sources within the subduction zone. However, the similarity of $\delta^{34}S$ values
898 to known Alpine hydrothermal pyrite (Garuti et al., 2009), and the appearance of $\delta^{34}S$
899 values around 7‰ in several of the samples studied, lead us to prefer a subduction-
900 mobilised hydrothermal source in the absence of other evidence to support a mixed
901 fluid source.
902
903 The heavier mode of pyrite, with $\delta^{34}S$ around 12‰ requires a source of sulfate within
904 the subduction zone, because such heavy $\delta^{34}S$ values cannot be derived from any
905 known sulfide inputs into subduction zones (Fig. 9A,B). Anhydrite occurs in the
906 sheeted dyke complex of the ocean crust (Alt and Shanks, 2003), but its subsequent
907 fate is not well known. Anyhdrite has retrograde solubility so it may be redissolved
908 by off-axis hydrothermal circulation (Alt and Shanks, 2003). However, anhydrite is
909 preserved in gabbroic units in ODP hole 504B (Alt, 1995), and in the Macquarie
910 Island ophiolite, suggesting that at least some anhydrite survives past the cessation of
911 hydrothermal circulation (Alt et al., 2003). Additional alteration as the slab bends
912 during initial subduction has been proposed by Ranero and Sallares (2004) and this
913 process could result in ocean floor entering subduction zones with higher sulfate and
914 sulfide content than that attained after on-axis and off-axis alteration. Anhydrite has a
915 number of high pressure polymorphs (Gracia et al., 2012) and may therefore survive
916 to great depths in the subducted slab, although there are no reports of anhydrite in

917 exhumed high pressure rocks. The lack of observations could, however, be due to the
918 high solubility of anhydrite in cold aqueous fluids, so that anhydrite in high pressure
919 rocks is dissolved in either the weathering environment or during sample preparation.
920
921 Sulfate at depth may also be sourced from supercritical melts with compositions
922 intermediate between silicate melts and aqueous fluids. Multi-phase solid inclusions
923 in UHP rocks from Dabie Shan with alkali-alumino silicate bulk compositions include
924 sulfate daughter minerals (Frezzotti and Ferrando, 2007). These inclusions are
925 interpreted as a record of supercritical hydro-silicate melts, and appear capable of
926 sulfate transport under UHP conditions in concentrations in excess of those for
927 aqueous fluids extrapolated from (Newton and Manning, 2005). Harlov and Hansen
928 (2005) propose infiltration of an oxidised, sulfate bearing, concentrated brine into
929 amphibolite and granulite facies rocks in Tamil Nadu, southern India, at lower crustal
930 pressure-temperature conditions, and such a fluid could exsolve from a supercritical
931 melt. However, it is likely that such a fluid would be diluted, buffered and re-
932 equilibrated in transit from the depths of formation to the rocks of interest. Such a
933 fluid is therefore considered to make a minor contribution to the sulfur isotope budget
934 during blueschist retrogression.
935
936 Pyrite precipitated from sulfate originally derived from hydrothermal pyrite could
937 also have a sulfur isotope signature as heavy, or heavier, than 12‰ (Fig. 9A,B).
938 However, sulfate is unlikely to have been the stable sulfur-bearing ligand if solutions
939 were rock-buffered, and if it were present then reduction of the sulfate to form sulfide
940 should have caused oxidation within the host rock. Such oxidation, in the form of
941 hematite or magnetite was sought carefully in the thin sections, but was not found. If

942 significant fluids did infiltrate from juxtaposed anhydrite- or pyrite-bearing sediments
943 with a heavy $\delta^{34}S$ signature within a subduction melange, then the 12‰ signature
944 could have been produced by fluids derived from these sediments as they became
945 reduced during interaction with the Pfülwe basalts (Wagner and Boyce, 2006). This
946 mechanism requires relatively close proximity of the sediment-basalt interface to the
947 samples because the oxidised sulfur would be dumped close to the interface.
948 However, the Pfülwe basalts are not close, at the present time, to suitable sediment
949 candidates so, while this possibility cannot be eliminated, it is deemed relatively
950 unlikely. Further study of other stable isotopes may allow the potential role of fluids
951 derived from low-grade sediments to be better constrained.
952
953 The presence of two different sources for sulfur in the pyrite associated with
954 blueschist retrogression raises the possibility that fluid mixing occurred during fluid
955 infiltration and pyrite precipitation. Fluid mixing, with varying proportions of fluids
956 from different sources, could explain the bimodal sulfur isotope distributions in the
957 Pfülwe samples (Fig. 3C, D, E), cyclical Co zoning (Fig. 4F, 5B, 6B, 7B) and periods
958 of resorption (Fig. 5B). It could also provide a way to trigger pyrite precipitation, by,
959 for example, changing redox or pH so that fluids entered the pyrite stability field.
960 Mixing could involve fluids from different sources, for example, basalt-derived and
961 sediment-derived, or sediment-derived and ultramafic-derived, or it could involve
962 mixing between an internally- and externally-derived fluid. The proposal of fluid
963 mixing is difficult to reconcile with the physical difficulty of mixing fluids that travel
964 on different flow paths and that are likely to have different densities. However,
965 during deformation, fluids migrate to lower pressure domains, such as the garnet
966 pressure shadows in ATPF-004, or into larger scale structural features. These lower-

967 pressure regions are points where fluids from different sources can collect or pause,
968 with time to chemically equilibrate with the rock, as they pass through a given
969 structural system. The dramatic changes in deformation and fluid pressure expected to
970 in a malfunctioning subduction zone, might provide the appropriate settings where
971 fluids from different sources could migrate through the same structural pathways.
972 Alternatively, the observed features may record sequential infiltration of fluids from
973 different sources rather than in-situ fluid mixing. Further work is necessary to assess
974 the possibility of fluid mixing and to constrain possible fluid sources.
975
976 ***5.9 Greenschist Retrogression***
977 Sulfides are associated with greenschist retrogressive minerals such as actinolite and
978 chlorite in almost all samples, but there is no distinctive isotopic signature that can be
979 associated uniquely with the greenschist mineral assemblage. Total sulfur modes are
980 no higher in the most retrogressed Pfülwe sample, PF0005, than in the least
981 retrogressed sample, ATPF-004. As a result, we conclude that sulfur addition
982 associated with greenschist retrogression may have been minor. It is therefore
983 possible that greenschist retrogression and fluid infiltration redistributed existing
984 sulfur on a scale similar to that of a thin section rather than involving infiltration of
985 sulfur from a different source. However, it may also be that sulfur was mobile on
986 length scales greater than that of the thin sections studied, but with similar sulfur
987 sources, and therefore sulfur isotope signatures, to the sulfur already present within
988 the rock.
989
990 A number of fluid sources become available as exhumation progresses. If
991 exhumation at the continental side of the subduction zone occurs synchronously with

992 the final stages of subduction at the oceanic side of the subduction zone (Babist et al.,
993 2006; Glodny et al., 2008), then exhuming rocks (e.g. ZS on Fig. 10C) could be
994 infiltrated by fluids from rocks that are still undergoing prograde heating and
995 devolatilisation. Rocks undergoing exhumation that are still partially hydrated can
996 release fluid on exhumation if the pressure-temperature path intersects dehydration
997 reactions from the low temperature side. This process has been invoked for local
998 greenschist retrogression in high pressure Alpine rocks from Corsica (Miller and
999 Cartwright, 2006). Additionally, exhuming rocks may be subcreted to the overlying
1000 plate and come into contact with less metamorphosed rocks where fluids liberated
1001 from lower grade rocks could contribute towards greenschist rehydration (Fry and
1002 Barnicoat, 1987).
1003
1004 ***5.10 In-Slab Sulfur Cycling***
1005 Heterogeneously distributed sulfides in the areas studied suggest that the slab can
1006 undergo sulfur addition in locally enriched high fluid flux domains. Since this
1007 remineralisation of the slab precipitates pyrite, there is opportunity for subsequent
1008 metamorphism and re-liberation of sulfur. The subduction zone sulfur system may be
1009 therefore something like a leaky loop, with repeated recycling of sulfur by downward
1010 subduction of pyrite, devolatilisation and loss of sulfur to upwards moving fluids, and
1011 then re-pyritisation of the slab to complete the loop. Loss of sulfur to the subduction
1012 channel and mantle wedge must occur to some extent; in fact, slab-derived sulfur is
1013 reported in metasomatised mantle xenoliths (McInnes et al., 2001).
1014
1015 ***5.11 Comparison of Alpine and New Caledonia samples***

1016 The Alpine and New Caledonia field areas are inferred to have reached similar peak
1017 temperatures but pressures are inferred to have been higher in the Zermatt-Saas
1018 (Barnicoat, 1985; Barnicoat and Fry, 1987; Carson et al., 1999; Fitzherbert et al.,
1019 2003; Reinecke, 1998), implying that the New Caledonia subduction zone had a
1020 higher geothermal gradient and that the New Caledonian samples did not penetrate so
1021 far into the subduction zone as the Alpine samples before exhumation.
1022
1023 Many features of samples from the two localities are similar; metabasalts from both
1024 areas contain typical magmatic sulfide assemblages (e.g. LC004, inclusions in garnet
1025 in EH-033) though these are inferred to have experienced prograde sulfidation in the
1026 Zermatt-Saas sample LC004. Both samples contain a significant proportion of pyrite
1027 inferred to be originally of hydrothermal origin, with some component of
1028 recrystallization and possible extra sulfur addition during retrogression. Matrix
1029 pyrites in New Caledonia samples have similar $\delta^{34}S$ to that of the inferred
1030 hydrothermal mode in the Zermatt-Saas samples, around 7‰, and a similar late
1031 textural setting. Similar processes may therefore be inferred to have formed these
1032 pyrites. A significant difference is that the $\delta^{34}S$ values around 12‰ found in the
1033 Pfülwe samples are not found in the New Caledonia samples. However, only one
1034 sample from New Caledonia was analysed so it would be premature to attribute this
1035 omission to any particular fundamental geological differences between the two
1036 subduction zones.
1037

1038 **6. Conclusions**

1039 To summarise, the combination of in-situ sulfur isotope micro analysis and trace
1040 elemental mapping with detailed petrological and textural analysis provides

significant new information on the sources and geometry of fluid flow during subduction and exhumation and on the systematics of sulfur cycling in subduction zones. Since sulfur isotope modification post crystallisation is relatively minor or non-existent, records of processes ranging from magmatic crystallisation, through hydrothermal alteration to blueschist and greenschist retrogression are retained. Pyrite crystallisation associated with blueschist retrogression requires two sulfur sources, one consistent with derivation from oceanic hydrothermal pyrite, and the other with a sulfate source. The most likely source of fluids that carry this sulfur is mineral devolatilisation from deeper within the slab. Fluid infiltration may have been facilitated by deformation associated with the beginning of exhumation. If this sequence of events is correct, then the observations of isotopically heavy sulfur in blueschist facies pyrite is evidence that anhydrite can be preserved to substantial depths and may contribute oxidised sulfur to the sub-arc mantle. However, alternative sources of fluids, such as locally-derived fluids liberated when exhumation pressure-temperature paths cross dehydration reactions from the low temperature side during decompression, and fluids produced by juxtaposition of exhuming rocks with lower grade rocks in the overlying plate, cannot be excluded. Further work is required to constrain the role of locally and externally derived fluids, and to quantify the contributions made by the different sulfur sources.

7. Acknowledgements

Boswell Wing is thanked for laser fluorination measurements of Sonora-3, pyrrhotite and chalcopyrite samples at McGill University. The authors acknowledge the facilities, and the scientific and technical assistance of the Australian Microscopy & Microanalysis Research Facility at the Centre for Microscopy, Characterisation &

Analysis, the University of Western Australia, a facility funded by the University, State and Commonwealth Governments. KE thanks the Australian Research Council for grants DP1094075 and FT120100579 that contributed towards this research. This is TiGeR paper number xxxx, and contribution XXX from the ARC Centre of Excellence for Core to Crust Fluid Systems (http://www.ccfs.mq.edu.au). Sonia Aulbach and an anonymous reviewer are thanked for comments that helped to improve the manuscript.

8. References

Aitchison, J.C., Clarke, G.L., Meffre, S., Cluzel, D., 1995. Eocene arc-continent collision in New Caledonia and implications for regional southwest Pacific tectonic evolution. Geology, 23(2): 161-164.

Alirezaei, S., Cameron, E.M., 2001. Variations of sulfur isotopes in metamorphic rocks from Bamble Sector, southern Norway: a laser probe study. Chemical Geology, 181(1-4): 23-45.

Alt, J.C., 1995. Sulfur isotopic profile through the oceanic-crust - sulfur mobility and seawater-crustal sulfur exchange during hydrothermal alteration. Geology, 23(7): 585-588.

Alt, J.C., 2003. Hydrothermal fluxes at mid-ocean ridges and on ridge flanks. Comptes Rendus Geoscience, 335(10-11): 853-864.

Alt, J.C., Davidson, G.J., Teagle, D.A.H., Karson, J.A., 2003. Isotopic composition of gypsum in the Macquarie Island ophiolite: Implications for the sulfur cycle and the subsurface biosphere in oceanic crust. Geology, 31(6): 549-552.

1091 Alt, J.C., Shanks, W.C., 2003. Serpentinization of abyssal peridotites from the MARK
1092 area, Mid-Atlantic Ridge: Sulfur geochemistry and reaction modeling.
1093 Geochimica Et Cosmochimica Acta, 67(4): 641-653.
1094 Alt, J.C. et al., 2007. Hydrothermal alteration and microbial sulfate reduction in
1095 peridotite and gabbro exposed by detachment faulting at the Mid-Atlantic
1096 Ridge, 15 degrees 20 ' N (ODP Leg 209): A sulfur and oxygen isotope study.
1097 Geochemistry Geophysics Geosystems, 8.
1098 Angiboust, S., Agard, P., Jolivet, L., Beyssac, O., 2009. The Zermatt-Saas ophiolite:
1099 the largest (60-km wide) and deepest (c. 70-80 km) continuous slice of
1100 oceanic lithosphere detached from a subduction zone? Terra Nova, 21(3): 171-
1101 180.
1102 Aulbach, S. et al., 2010. Granulite sulphides as tracers of lower crustal origin and
1103 evolution: An example from the Slave craton, Canada. Geochimica Et
1104 Cosmochimica Acta, 74(18): 5368-5381.
1105 Aulbach, S., Stachel, T., Seitz, H.-M., Brey, G.P., 2012. Chalcophile and siderophile
1106 elements in sulphide inclusions in eclogitic diamonds and metal cycling in a
1107 Paleoproterozoic subduction zone. Geochimica Et Cosmochimica Acta, 93:
1108 278-299.
1109 Babist, J., Handy, M.R., Konrad-Schmolke, M., Hammerschmidt, K., 2006.
1110 Precollisional, multistage exhumation of subducted continental crust: The
1111 Sesia Zone, western Alps. Tectonics, 25(6).
1112 Barley, M.E., Krapez, B., Groves, D.I., Kerrich, R., 1998. The Late Archaean
1113 bonanza: metallogenic and environmental consequences of the interaction
1114 between mantle plumes, lithospheric tectonics and global cyclicity.
1115 Precambrian Research, 91(1-2): 65-90.

1116 Barnicoat, A.C., 1985. High-pressure metamorphism in the Zermatt-Saas zone of the
1117 Swiss Alps. Journal of the Geological Society, 142: 1243-1243.
1118 Barnicoat, A.C., Fry, N., 1987. Eoalpine high-pressure metamorphism in the Western
1119 Alps. Journal of the Geological Society, 144: 521-521.
1120 Barton, P.B., Jr., Toulmin, P., III, 1964a. The electrum-tarnish method for the
1121 determination of the fugacity of sulfur in laboratory sulfide sytstems.
1122 Geochemica et Cosmochimica Acta, 28: 619-640.
1123 Barton, P.B., Jr., Toulmin, P., III, 1964b. Experimental determination of the reaction
1124 chalcopyrite + sulfur = pyrite + bornite from 350 to 500 degrees C. Economic
1125 Geology and the Bulletin of the Society of Economic Geologists, 59: 747-752.
1126 Bell, T.H., Brothers, R.N., 1985. Development of P-T prograde and P-retrograde, T-
1127 prograde isogradic surfaces during blueschist to eclogite regional deformation
1128 metamorphism in New Caledonia, as indicated by progressively developed
1129 porphyroblast microstructures. Journal of Metamorphic Geology, 3(1): 59-78.
1130 Beltrando, M., Rubatto, D., Manatschal, G., 2010. From passive margins to orogens:
1131 The link between ocean-continent transition zones and (ultra)high-pressure
1132 metamorphism. Geology, 38(6): 559-562.
1133 Benning, L.G., Seward, T.M., 1996. Hydrosulphide complexing of Au(I) in
1134 hydrothermal solutions from 150-400 degrees C and 500-1500 bar.
1135 Geochimica et Cosmochimica Acta, 60(11): 1849-1871.
1136 Black, P.M., 1977. Regional high-pressure metamorphism in New Caledonia - phase-
1137 equilibria in Ouegoa district. Tectonophysics, 43(1-2): 89-107.
1138 Bocquet, J., Delaloye, M., Hunziker, J.C., Krummena.D, 1974. K-Ar and Rb-Sr
1139 dating of blue amphiboles, micas, and associated minerals from Western Alps.
1140 Contributions to Mineralogy and Petrology, 47(1): 7-26.

1141 Briggs, R.M., Kobe, H.W., Black, P.M., 1977. High-pressure metamorphism of
1142 stratiform sulfide deposits from Diahot Region, New Caledonia. Mineralium
1143 Deposita, 12(3): 263-279.
1144 Brown, J., 2007. The deep sulfur cyle: Insights from prograde sulfide metamorphism
1145 in
1146 blueschist and eclogite, northeastern New Caledonia., Australian National University.
1147 Cabral, R.A. et al., 2013. Anomalous sulphur isotopes in plume lavas reveal deep
1148 mantle storage of Archaean crust. Nature, 496(7446): 490-+.
1149 Canfield, D.E., 2001. Isotope fractionation by natural populations of sulfate-reducing
1150 bacteria. Geochimica Et Cosmochimica Acta, 65(7): 1117-1124.
1151 Canfield, D.E., 2004. The evolution of the Earth surface sulfur reservoir. American
1152 Journal of Science, 304(10): 839-861.
1153 Canfield, D.E., Poulton, S.W., Narbonne, G.M., 2007. Late-Neoproterozoic deep-
1154 ocean oxygenation and the rise of animal life. Science, 315(5808): 92-95.
1155 Carson, C.J., Powell, R., Clarke, G.L., 1999. Calculated mineral equilibria for
1156 eclogites in CaO-Na2O-FeO-MgO-Al2O3-SiO2-H2O: application to the
1157 Pouebo Terrane, Pam Peninsula, New Caledonia. Journal of Metamorphic
1158 Geology, 17(1): 9-24.
1159 Clarke, G.L., Aitchison, J.C., Cluzel, D., 1997. Eclogites and blueschists of the Pam
1160 Peninsula, NE New Caledonia: A reappraisal. Journal of Petrology, 38(7):
1161 843-876.
1162 Cluzel, D., Aitchison, J., Clarke, G., Meffre, S., Picard, C., 1995. Tectonic unroofing
1163 of the Tertiary high-pressure metamorphic core complex of Northern New-
1164 Caledonia - a kinematic analysis. Comptes Rendus De L Academie Des

1165 Sciences Serie Ii Fascicule a-Sciences De La Terre Et Des Planetes, 321(1):
1166 57-64.
1167 Dale, C.W. et al., 2009. Highly siderophile element behaviour accompanying
1168 subduction of oceanic crust: Whole rock and mineral-scale insights from a
1169 high-pressure terrain. Geochimica Et Cosmochimica Acta, 73(5): 1394-1416.
1170 Evans, K.A., 2010. A test of the viability of fluid–wall rock interaction mechanisms
1171 for changes in opaque phase assemblage in metasedimentary rocks in the
1172 Kambalda-St. Ives goldfield, Western Australia. Mineralium Deposita, 45(2):
1173 207-213.
1174 Evans, K.A., 2012. The redox budget of subduction zones. Earth Science Reviews,
1175 113: 11-32.
1176 Evans, K.A., Elburg, M.A., Kamenetsky, V.S., 2012. The oxidation state of sub-arc
1177 mantle. Geology, 40: 783-786.
1178 Evans, K.A., Phillips, G.N., Powell, R., 2006. Rock-buffering of auriferous fluids in
1179 altered rocks associated with the Golden Mile-style mineralization, Kalgoorlie
1180 gold field, Western Australia. Economic Geology, 101(4): 805-817.
1181 Evans, K.A., Tomkins, A., 2011. The relationship between subduction zone redox
1182 budget and arc magma fertility. Earth and Planetary Science Letters, 308: 401-
1183 409.
1184 Farquhar, J. et al., 2013. Pathways for Neoarchean pyrite formation constrained by
1185 mass-independent sulfur isotopes. Proceedings of the National Academy of
1186 Sciences, 110: 17638-43.
1187 Farquhar, J., Wu, N.P., Canfield, D.E., Oduro, H., 2010. Connections between sulfur
1188 cycle evolution, sulfur isotopes, sediments, and base metal sulfide deposits.
1189 Economic Geology, 105(3): 509-533.

1190 Fitzherbert, J.A., Clarke, G.L., Powell, R., 2003. Lawsonite-omphacite-bearing
1191 metabasites of the Pam Peninsula, NE New Caledonia: Evidence for disrupted
1192 blueschist- to eclogite-facies conditions. Journal of Petrology, 44(10): 1805-
1193 1831.
1194 Frezzotti, M.L., Ferrando, S., 2007. Multiphase solid inclusions in ultrahigh-pressure
1195 metamorphic rocks: a petrographic approach. Periodico Di Mineralogia, 76(2-
1196 3): 113-125.
1197 Frezzotti, M.L., Selverstone, J., Sharp, Z.D., Compagnoni, R., 2011. Carbonate
1198 dissolution during subduction revealed by diamond-bearing rocks from the
1199 Alps. Nature Geoscience, 4(10): 703-706.
1200 Fry, N., Barnicoat, A.C., 1987. The tectonic implications of high-pressure
1201 metamorphism in the Western Alps. Journal of the Geological Society, 144:
1202 653-659.
1203 Garuti, G., Alfonso, P., Proenza, J.A., Zaccarini, F., 2009. Sulfur-isotope variations in
1204 sulfide minerals from massive sulfide deposits of the Northern Apennine
1205 ophiolites: inorganic and biogenic constraints. Ofioliti, 34(1): 43-62.
1206 Glodny, J., Ring, U., Kuhn, A., 2008. Coeval high-pressure metamorphism, thrusting,
1207 strike-slip, and extensional shearing in the Tauern Window, Eastern Alps.
1208 Tectonics, 27(4).
1209 Gracia, L., Beltran, A., Errandonea, D., Andres, J., 2012. CaSO4 and Its Pressure-
1210 Induced Phase Transitions. A Density Functional Theory Study. Inorganic
1211 Chemistry, 51(3): 1751-1759.
1212 Grinenko, V.A., Dmitriev, L.V., Migdisov, A.A., Sharas'kin, A.Y., 1975. Sulfur
1213 contents and isotope compositions for igneous and metamorphic rocks from
1214 mid-ocean ridges. Geokhimiya, 2: 199-206.

1215 Harlov, D.E., Hansen, E.C., 2005. Oxide and sulphide isograds along a Late Archean,
1216 deep-crustal profile in Tamil Nadu, south India. Journal of Metamorphic
1217 Geology, 23(4): 241-259.
1218 Hartmann, G., Wedepohl, K.H., 1993. The composition of peridotite tectonites from
1219 the Ivrea Complex, Northern Italy - residues from melt extraction. Geochimica
1220 Et Cosmochimica Acta, 57(8): 1761-1782.
1221 Healy, D., Reddy, S.M., Timms, N.E., Gray, E.M., Brovarone, A.V., 2009. Trench-
1222 parallel fast axes of seismic anisotropy due to fluid-filled cracks in subducting
1223 slabs. Earth and Planetary Science Letters, 283(1-4): 75-86.
1224 Hilton, D.R., Fischer, T.P., Marty, B., 2002. Noble gases and volatile recycling at
1225 subduction zones, Noble Gases in Geochemistry and Cosmochemistry.
1226 Reviews in Mineralogy & Geochemistry, pp. 319-370.
1227 Itaya, T., Brothers, R.N., Black, P.M., 1985. Sulfides, oxides and sphene in high-
1228 pressure schists from New Caledonia. Contributions to Mineralogy and
1229 Petrology, 91(2): 151-162.
1230 Jego, S., Pichavant, M., Mavrogenes, J.A., 2010. Controls on gold solubility in arc
1231 magmas: An experimental study at 1000 degrees C and 4 kbar. Geochimica Et
1232 Cosmochimica Acta, 74(7): 2165-2189.
1233 Jenner, F.E., O'Neill, H.S.C., Arculus, R.J., Mavrogenes, J.A., 2010. The magnetite
1234 crisis in the evolution of arc-related magmas and the initial concentration of
1235 Au, Ag and Cu. Journal of Petrology, 51(12): 2445-2464.
1236 Kawakami, T., Ellis, D.J., Christy, A.G., 2006. Sulfide evolution in high-temperature
1237 to ultrahigh-temperature metamorphic rocks from Lutzow-Holm Complex,
1238 East Antarctica. Lithos, 92(3-4): 431-446.

1239 Kelley, K.A., Cottrell, E., 2009. Water and the oxidation state of subduction zone
1240 magmas. Science, 325(5940): 605-607.
1241 Kendrick, M.A., Scambelluri, M., Honda, M., Phillips, D., 2011. High abundances of
1242 noble gas and chlorine delivered to the mantle by serpentinite subduction.
1243 Nature Geoscience, 4(11): 807-812.
1244 Kita, N.T., Ushikubo, T., Fu, B., Valley, J.W., 2009. High precision SIMS oxygen
1245 isotope analysis and the effect of sample topography. Chemical Geology,
1246 264(1-4): 43-57.
1247 Leach, D.L. et al., 2010. Sediment-hosted lead-zinc deposits in Earth history.
1248 Economic Geology, 105(3): 593-625.
1249 Li, X.P., Rahn, M., Bucher, K., 2004. Serpentinites of the Zermatt-Saas ophiolite
1250 complex and their texture evolution. Journal of Metamorphic Geology, 22(3):
1251 159-177.
1252 Liu, W. et al., 2011. Speciation and thermodynamic properties for cobalt chloride
1253 complexes in hydrothermal fluids at 35-440 degrees C and 600 bar: An in-situ
1254 XAS study. Geochimica Et Cosmochimica Acta, 75(5): 1227-1248.
1255 Marini, L., Moretti, R., Accornero, M., 2011. Sulfur isotopes in magmatic-
1256 hydrothermal systems, melts, and magmas, Sulfur in Magmas and Melts: Its
1257 Importance for Natural and Technical Processes. Reviews in Mineralogy &
1258 Geochemistry, pp. 423-492.
1259 Martin, S., Rebay, G., Kienast, J.-R., Mevel, C., 2008. An eclogitised oceanic palaeo-
1260 hydrothermal field from the St. Marcel Valley (Italian Western Alps). Ofioliti,
1261 33(1): 49-63.
1262 McClay, K.R., Ellis, P.G., 1983. Deformation and recrystallization of pyrite.
1263 Mineralogical Magazine, 47(345): 527-538.

McInnes, B.I.A., Gregoire, M., Binns, R.A., Herzig, P.M., Hannington, M.D., 2001. Hydrous metasomatism of oceanic sub-arc mantle, Lihir, Papua New Guinea: petrology and geochemistry of fluid-metasomatised mantle wedge xenoliths. Earth and Planetary Science Letters, 188(1-2): 169-183.

Migdisov, A.A., Zezin, D., Williams-Jones, A.E., 2011. An experimental study of Cobalt (II) complexation in Cl- and H2S-bearing hydrothermal solutions. Geochimica Et Cosmochimica Acta, 75(14): 4065-4079.

Miller, D.J., Cervantes, P., 2002. Sulfide mineral chemistry and petrography and platinum group element composition in gabbroic rocks from the southwest Indian ridge. In: Natland, J.H., Dick, H.J.R., Miller, D.J., Von Herzen, R.P. (Eds.), Proceedings of the Ocean Drilling Program, Scientific Results, pp. 1-29.

Miller, J.A., Cartwright, I., 2006. Albite vein formation during exhumation of high-pressure terranes: a case study from alpine Corsica. Journal of Metamorphic Geology, 24(5): 409-428.

Mottl, M.J., Wheat, C.G., Fryer, P., Gharib, J., Martin, J.B., 2004. Chemistry of springs across the Mariana forearc shows progressive devolatilization of the subducting plate. Geochimica Et Cosmochimica Acta, 68(23): 4915-4933.

Mungall, J.E., Hanley, J.J., Arndt, N.T., Debecdelievre, A., 2006. Evidence from meimechites and other low-degree mantle melts for redox controls on mantle-crust fractionation of platinum-group elements. Proceedings of the National Academy of Sciences of the United States of America, 103(34): 12695-12700.

Newton, R.C., Manning, C.E., 2005. Solubility of anhydrite, CaSO4, in NaCl-H2O solutions at high pressures and temperatures: Applications to fluid-rock interaction. Journal of Petrology, 46(4): 701-716.

1289 Ohmoto, H., Goldhaber, M.B., 1997. Applications of sulfur and carbon isotopes in ore
1290 deposit research. In: Barnes, H.L. (Ed.), Geochemistry of hydrothermal ore
1291 deposits. Wiley, New York, pp. 517-611.
1292 Ohmoto, H., Hayashi, K., Kajisa, Y., 1994. EXPERIMENTAL-STUDY OF THE
1293 SOLUBILITIES OF PYRITE IN NACL-BEARING AQUEOUS-
1294 SOLUTIONS AT 250-350-DEGREES-C. Geochimica Et Cosmochimica
1295 Acta, 58(10): 2169-2185.
1296 Ohmoto, H., Rye, R.O., 1979. Isotopes of sulfur and carbon. In: Barnes, H.L. (Ed.),
1297 Geochemistry of Hydrothermal Ore Deposits. John Wiley and Sons, New
1298 York, pp. 509-567.
1299 Padron-Navarta, A.J. et al., 2010. Fluid transfer into the wedge controlled by high-
1300 pressure hydrofracturing in the cold top-slab mantle. Earth and Planetary
1301 Science Letters, 297(1-2): 271-286.
1302 Philippot, P., Selverstone, J., 1991. Trace-element-rich brines in eclogitic veins -
1303 implications for fluid composition and transport during subduction.
1304 Contributions to Mineralogy and Petrology, 106(4): 417-430.
1305 Pokrovski, G.S., Dubrovinsky, L.S., 2011. The S-3(-) ion Is stable in geological fluids
1306 at elevated temperatures and pressures. Science, 331(6020): 1052-1054.
1307 Pokrovski, G.S., Tagirov, B.R., Schott, J., Hazemann, J.-L., Proux, O., 2009. A new
1308 view on gold speciation in sulfur-bearing hydrothermal fluids from in situ X-
1309 ray absorption spectroscopy and quantum-chemical modeling. Geochimica Et
1310 Cosmochimica Acta, 73(18): 5406-5427.
1311 Puchelt, H., Prichard, H.M., Berner, Z., Maynard, J., 1996. Sulfide mineralogy, sulfur
1312 content, and sulfur isotope composition of mafic and ultramafic rocks from

1313 Leg 147. In: Mevel, C., Gillis, K.M., Allan, J.F., Meyer, P.S. (Eds.),
1314 Proceedings of the Ocean Drilling Program, Scientific Results. Vol 147.
1315 Ranero, C.R., Sallares, V., 2004. Geophysical evidence for hydration of the crust and
1316 mantle of the Nazca plate during bending at the north Chile trench. Geology,
1317 32(7): 549-552.
1318 Reed, M.H., Palandri, J., 2006. Sulfide mineral precipitation from hydrothermal
1319 fluids. Sulfide Mineralolgy and Geochemistry, 61: 609-631.
1320 Reinecke, T., 1991. Very-high-pressure metamorphism and uplift of coesite-bearing
1321 metasediments from the Zermatt-Saas Zone, Western Alps. European Journal
1322 of Mineralogy, 3(1): 7-17.
1323 Reinecke, T., 1998. Prograde high- to ultrahigh-pressure metamorphism and
1324 exhumation of oceanic sediments at Lago di Cignana, Zermatt-Saas Zone,
1325 western Alps. Lithos, 42(3-4): 147-189.
1326 Richards, J.P., 2011. Magmatic to hydrothermal metal fluxes in convergent and
1327 collided margins. Ore Geology Reviews, 40(1): 1-26.
1328 Rubatto, D., Gebauer, D., Fanning, M., 1998. Jurassic formation and Eocene
1329 subduction of the Zermatt-Saas-Fee ophiolites: implications for the
1330 geodynamic evolution of the Central and Western Alps. Contributions to
1331 Mineralogy and Petrology, 132(3): 269-287.
1332 Rudnick, R.L., Fountain, D.M., 1995. Nature and composition of the continental-crust
1333 - a lower crustal perspective. Reviews of Geophysics, 33(3): 267-309.
1334 Scambelluri, M., Philippot, P., 2001. Deep fluids in subduction zones. Lithos, 55(1-
1335 4): 213-227.

1336 Spandler, C., Hermann, J., 2006. High-pressure veins in eclogite from New Caledonia
1337 and their significance for fluid migration in subduction zones. Lithos, 89(1-2):
1338 135-153.
1339 Spandler, C., Hermann, J., Arculus, R., Mavrogenes, J., 2004. Geochemical
1340 heterogeneity and element mobility in deeply subducted oceanic crust; insights
1341 from high-pressure mafic rocks from New Caledonia. Chemical Geology,
1342 206(1-2): 21-42.
1343 Spandler, C., Pettke, T., Rubatto, D., 2011. Internal and external fluid sources for
1344 eclogite-facies veins in the Monviso meta-ophiolite, Western Alps:
1345 implications for fluid flow in subduction zones. Journal of Petrology, 52(6):
1346 1207-1236.
1347 Spandler, C., Rubatto, D., Hermann, R., 2005. Late Cretaceous-Tertiary tectonics of
1348 the southwest Pacific: Insights from U-Pb sensitive, high-resolution ion
1349 microprobe (SHRIMP) dating of eclogite facies rocks from New Caledonia.
1350 Tectonics, 24(3).
1351 Thomassot, E. et al., 2009. Metasomatic diamond growth: A multi-isotope study (C-
1352 13, N-15, S-33, S-34) of sulphide inclusions and their host diamonds from
1353 Jwaneng (Botswana). Earth and Planetary Science Letters, 282(1-4): 79-90.
1354 Tomkins, A.G., 2013. A biogeochemical influence on the secular distribution of
1355 orogenic gold. Economic Geology, 108: 193-197.
1356 Toulmin, P., III, Barton, P.B., Jr., 1964. Thermodynamic study of pyrite and
1357 pyrrhotite. Geochimica et Cosmochimica Acta, 28: 641-671.
1358 Ueda, A., Sakai, H., 1984. Sulfur isotope study of quaternary volcanic-rocks from the
1359 Japanese Islands Arc. Geochimica Et Cosmochimica Acta, 48(9): 1837-1848.

Wagner, T., Boyce, A.J., 2006. Pyrite metamorphism in the Devonian Hunsruck Slate of Germany: Insights from laser microprobe sulfur isotope analysis and thermodynamic modeling. American Journal of Science, 306(7): 525-552.

Wallace, P.J., Edmonds, M., 2011. The sulfur budget in magmas: evidence from melt inclusions, submarine glasses, and volcanic gas emissions, Sulfur in Magmas and Melts: Its Importance for Natural and Technical Processes. Reviews in Mineralogy & Geochemistry, pp. 215-246.

Walther, J.V., 1991. Determining the thermodynamic properties of solutes in crustal fluids. American Journal of Science, 291(5): 453-472.

Widmer, T., Thompson, A.B., 2001. Local origin of high pressure vein material in eclogite facies rocks of the Zermatt-Saas Zone, Switzerland. American Journal of Science, 301(7): 627-656.

Woodhead, J.D., Harmon, R.S., Fraser, D.G., 1987. O, S, Sr, and Pb isotope variations in volcanic-rocks from the Northern Mariana Islands - implications for crustal recycling in intraoceanic Arcs. Earth and Planetary Science Letters, 83(1-4): 39-52.

Zheng, Y.-F., 2009. Fluid regime in continental subduction zones: petrological insights from ultrahigh-pressure metamorphic rocks. Journal of the Geological Society, 166: 763-782.

Tables

Table 1: Summary of $\delta^{34}S$ sulfur isotope analyses

Grain	Phase	Group average $\delta^{34}S_{VCDT}$ (‰)	External group 1σ (‰)	Number of analyses	Average 1σ on single analysis (‰)
LC004					
LC004_002	pyrite	-7.39	0.20	15	0.21
LC003_002	pyrite	-6.68	n.a.	2	0.2
LC004-004	pyrite	-7.65	0.33	17	0.2
LC004-005	pyrite	-7.66	0.93	6	0.2
LC004-005	chalcopyrite	-13.72	2.76	3	0.2
LC004-005	pyrrhotite	-13.64	n.a.	2	0.2
LC008A					
LC008A-082	pyrite	-4.31	1.66	5	0.38
LC008A-0003	pyrite	-0.68	0.65	2	0.38
	pyrite	-4.10	0.32	2	0.38
LC008A-0006	pyrite	-0.61	3.08	4	0.39
LC008A-0007	pyrite	0.87	1.90	5	0.35
LC008A-0004	pyrite	-0.12	0.78	5	0.38
LC008A-0003b	pyrite	0.73	n.a.	1	0.37
LC008A-0008	pyrite	-0.48	1.97	5	0.37
	pyrite	-4.66	n.a.	1	0.39
LC008A-0005	pyrite	-0.74	0.43	6	0.25
LC008A-0008b	pyrite	-0.97	0.01	2	0.2
	pyrite	-4.13	n.a.	1	0.22
LC-008-001	pyrite	-0.21	0.12	4	0.24
PF005					
PF005-0015	pyrite	13.22	1.68	11	0.28
PF005-017	pyrite	12.54	1.97	10	0.28
	pyrite	5.28	n.a.	1	0.28
PF005-019	pyrite	11.76	0.73	7	0.26
	pyrite	3.18	0.24	2	0.56
PF005-0020	pyrite	12.40	0.75	7	0.27
	pyrite	5.41	2.50	3	0.28
PF005-0020B	pyrite	13.00	0.32	6	0.27
PF005-0022	pyrite	12.25	1.33	11	0.28
	pyrite	4.44	2.73	2	0.28
PF005-0018	pyrite	3.73	n.a.	1	0.32
PF008					
PF008-0024	pyrite	12.26	1.12	7	0.20
	pyrite	6.22	0.78	11	0.21
PF008-0027	pyrite	12.45	0.53	6	0.22
PF008-0026	pyrite	6.56	1.84	2	0.20
	pyrite	10.91	n.a.	1	0.26

PF008-0032	pyrite	7.15	0.28	6	0.22
PF008-0031	pyrite	6.88	n.a.	1	0.22
PF008-0024	chalcopyrite	0.52	n.a.	1	0.17
PF008-0028	chalcopyrite	12.50	n.a.	1	0.21
	pyrite	7.10	n.a.	1	0.30
ATPF004					
ATPF004-G1	pyrite	8.40	0.62	18	0.32
	pyrite	11.74	0.39	2	0.33
ATPF004-G2	pyrite	12.58	0.39	8	0.32
ATPF004-G3	pyrite	13.61	0.21	3	0.30
	pyrite	10.17	0.20	2	0.30
ATPF004-G4	pyrite	9.16	0.67	5	0.32
ATPF004-G5	pyrite	9.87	0.72	3	0.32
	pyrite	13.22	n.a.	1	0.33
EH033					
EH033-G1	pyrite	5.22	0.22	100	0.29 or 0.05
EH033-G2	pyrite	5.73	0.55	9	0.29

Figure Captions

Figure 1: Geological maps of sample localities: A) Zermaat-Saas zone, Western Alps. After Rebay et al. (2012); B) New Caledonia (Frost et al., 2013).

Figure 2: Photomicrographs of the sections used illustrating textural points: A, B: pyrite-pyrrhotite polysulfide grain associated with chlorite in LC004, ppl; B: rfl; C, D: chlorite and pyrite inclusions in inclusion-rich rim of garnet in LC008. C: PPL; D: XPL: E: pyrite inclusion in LC008; F: growth zoning and late rim on pyrite in LC008 revealed by tarnish pattern; G, H: Late polygranular, equant pyrite with tarnish delineating complex eccentric zoning in PF005, G: rfl, H: xpl; I, J: Equant pyrite grain in the matrix of PF008, overprinting the greenschist mineral assemblage, I: ppl; J:rfl; K, L: pyrite in matrix of ATPF-004 in contact with omphacite, K, ppl, L, rfl.

Figure 3: Histograms of $\delta^{34}S$ values. A) LC004; B) LC008A; C) PF005; D) PF008; E) ATPF004; F) EH033; G) EH033 high resolution analyses.

Figure 4. LC samples. A) reflected light photomicrograph of gold-coated sample LC004 showing the polysulfide grain LC004-005; B) trace element map of polysulfide grain LC004-005; C) reflected light photomicrograph of gold-coated sample LC004 showing the polysulfide grain LC004-004; D) reflected light photomicrograph of pyrites included in rim of garnet in sample LC008A, analyses shown are those from LC008A – 005; E) reflected light photomicrograph of gold coated sample LC008A showing pyrite grain LC008A-003; F) RGB image of Co (red and green to make yellow) and Fe (blue) for pyrite grain LC008A-003; G) reflected light photomicrograph of gold coated sample LC008A showing pyrite grain LC008A-

001; H) RGB image of Co (red and green to make yellow) and Fe (blue) for pyrite grain LC008A-001. All values are $\delta^{34}S$.

Figure 5: PF005: A) reflected light photomicrograph of PF005 showing pyrite grain PF005-020 and 020b; B) trace element map of pyrite grain PF005-020 and 020b. All values are $\delta^{34}S$.

Figure 6: PF008: A) trace element map of pyrite grain PF008-024; B) reflected light photomicrograph of pyrite-chalcopyrite grain PF008-027; C) reflected light photomicrograph of pyrite grain PF008-032; D) reflected light photomicrograph of gold coated sample showing grain PF008-028. All values are $\delta^{34}S$.

Figure 7: ATPF-004. Least retrogressed of the Pfulwe mafic samples. A) reflected light photomicrograph of gold coated sample showing grain ATPF-004 G1; B) Co map of grain ATPF-004 G1. Values are in wt%; C) $\delta^{34}S$ profile across ATPF004-G1; D) Sulfur isotope values superimposed on image of pyrite grain ATPF-004 G5 in gold coated sample. Grain lies in an embayment in garnet surrounded by retrogressive minerals. E) sulfur isotope values superimposed on image of pyrite grain ATPF-004 G3 in gold coated sample. Grain is in contact with garnet and is situated in an embayment into garnet.

Figure 8: EH033. A) photomicrograph of gold coated sample showing locations of analysis pits in pyrite grain G1; B) contoured map of $\delta^{34}S$ values in grain G1; C) Trace element map of Co content in grain G1; D) RGB image of Co (red and green to make yellow) and Fe (blue) in grain G1; D) Al maps of the vicinity of pyrite grain G1

showing location of clinozoisite; F) Na map of the vicinity of pyrite grain G1 showing location of barroisite and omphacite.

Figure 9: Calculated relationships between $\delta^{34}S$ and reaction progress for different pairs of sulfur compounds at 300ºC. A) Closed system equilibration; B) open system Rayleigh fractionation;

Figure 10: Schematic tectonic illustration of Alpine subduction and exhumation. Modified from Babist et al. (2006).

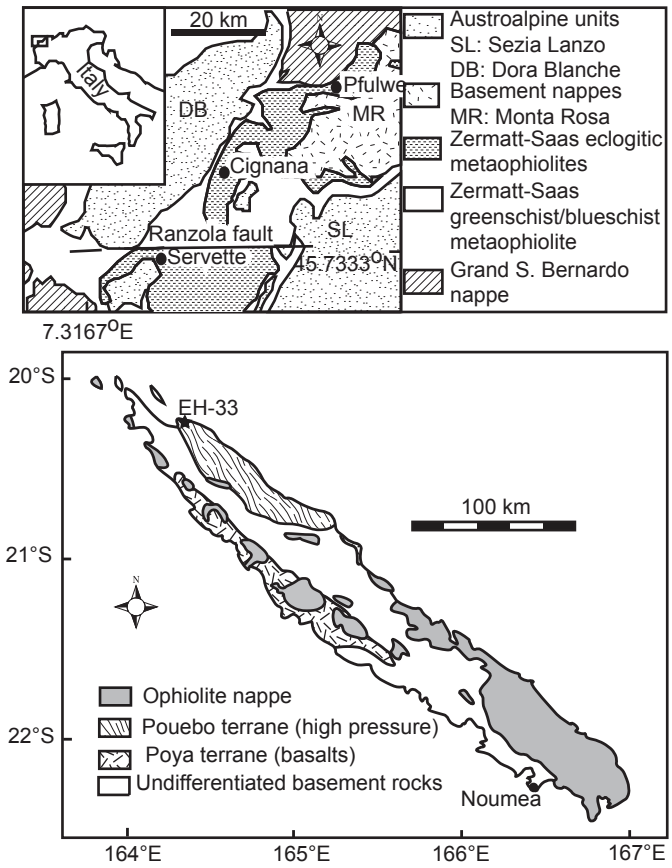
20 km
Italy
DB
Pfulwe
MR
Cignana
Ranzola fault
SL
Servette
45.7333°N
7.3167°E
Austroalpine units
SL: Sezia Lanzo
DB: Dora Blanche
Basement nappes
MR: Monta Rosa
Zermatt-Saas eclogitic metaophiolites
Zermatt-Saas greenschist/blueschist metaophiolite
Grand S. Bernardo nappe
20°S
21°S
22°S
EH-33
100 km
N
Ophiolite nappe
Pouebo terrane (high pressure)
Poya terrane (basalts)
Undifferentiated basement rocks
Noumea
164°E
165°E
166°E
167°E

Figure 1

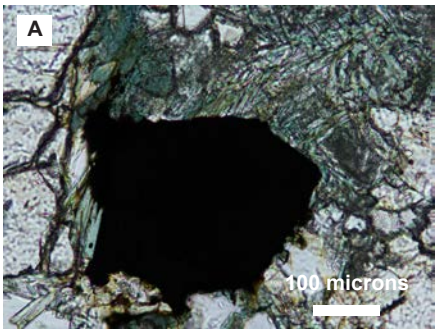
A
100 microns

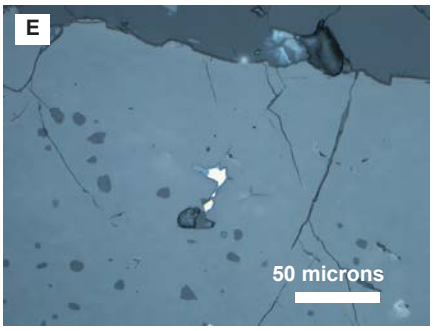
E
50 microns

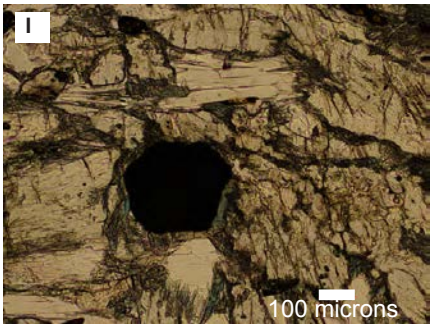
I
100 microns

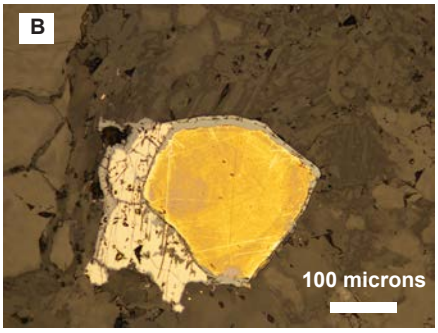
B
100 microns

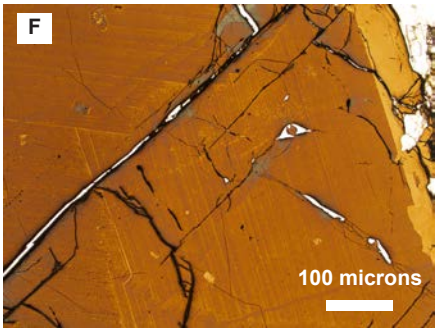
F
100 microns

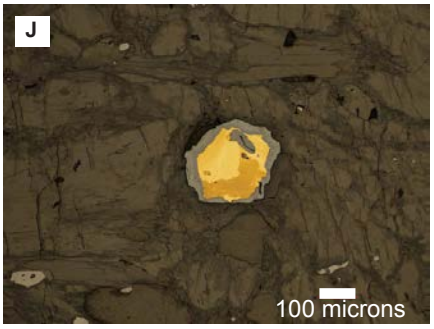
J
100 microns

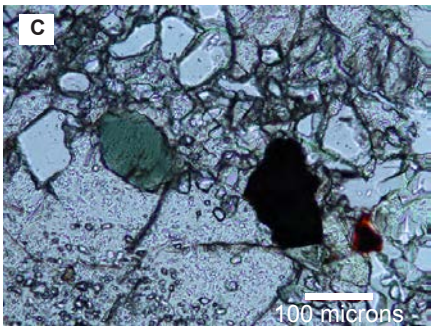
C
100 microns

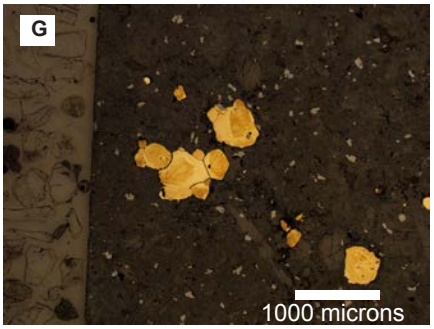
G
1000 microns

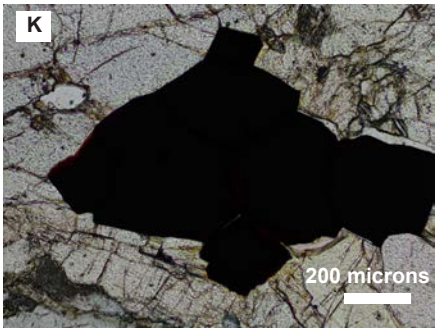
K
200 microns

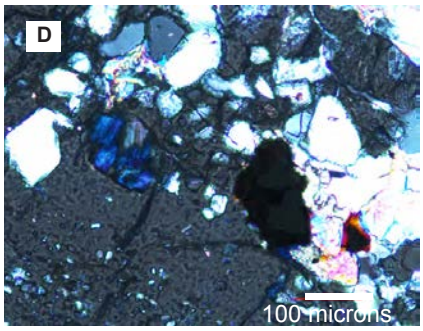
D
100 microns

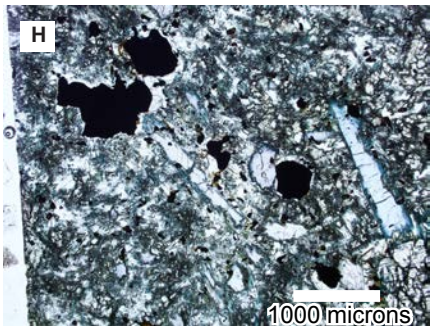
H
1000 microns

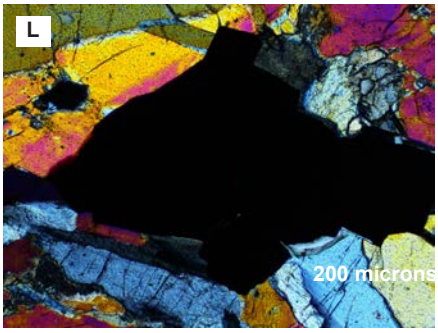
L
200 microns

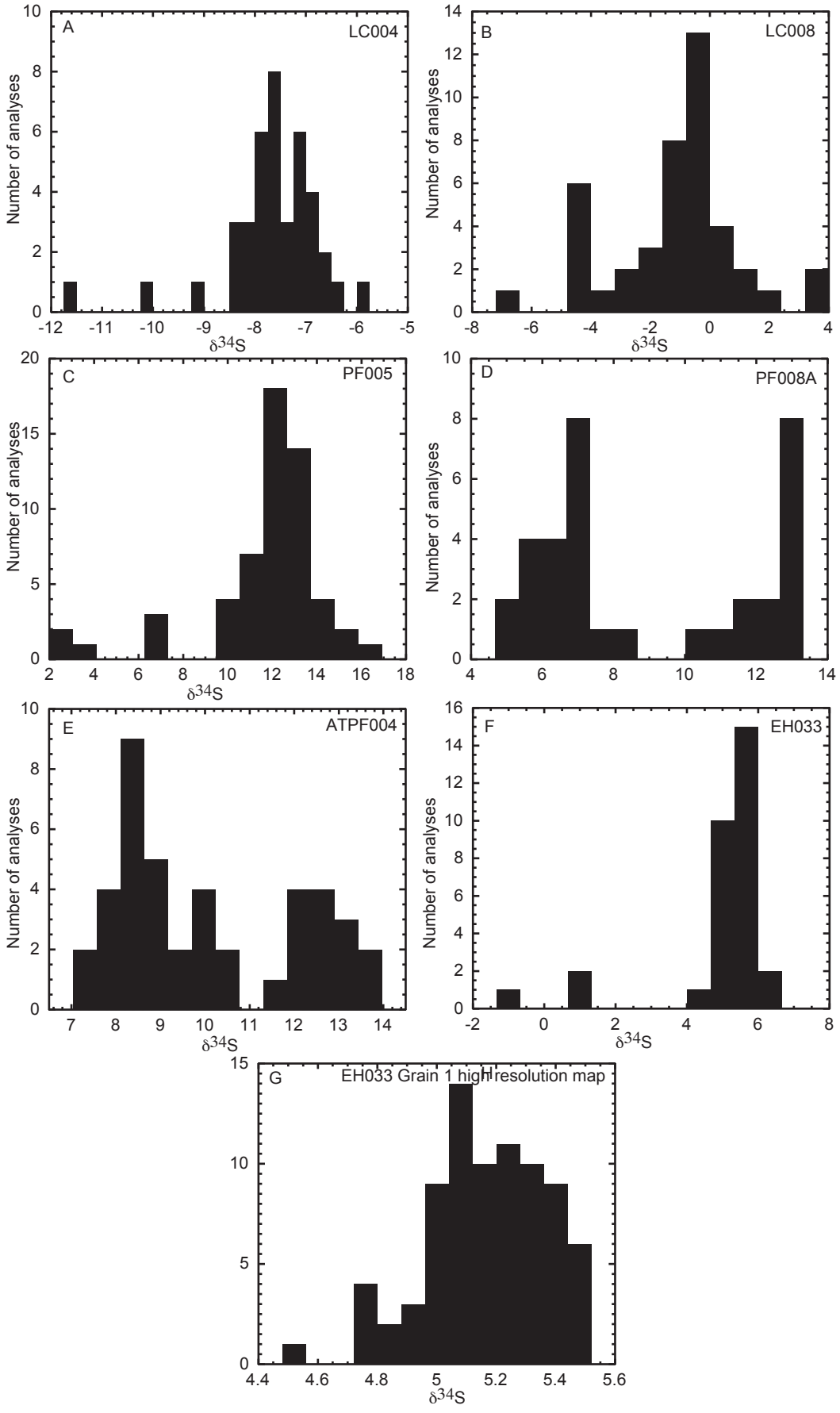
A
LC004
B
LC008
C
PF005
D
PF008A
E
ATPF004
F
EH033
G
EH033 Grain 1 high resolution map
Number of analyses
δ34S

Figure 3

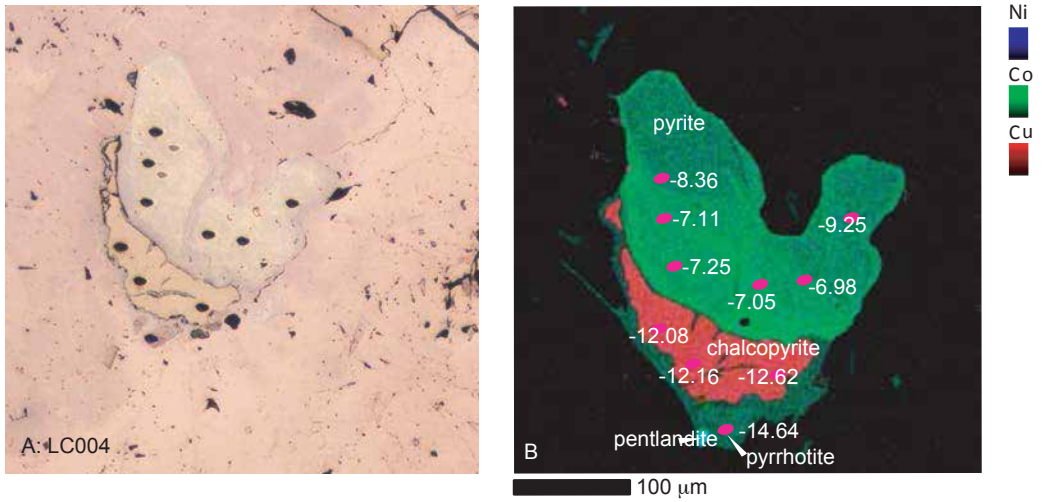
A: LC004
B
pyrite
-8.36
-7.11
-9.25
-7.25
-6.98
-7.05
-12.08
chalcopyrite
-12.16
-12.62
pentlandite
-14.64
pyrrhotite
Ni
Co
Cu
100 μm

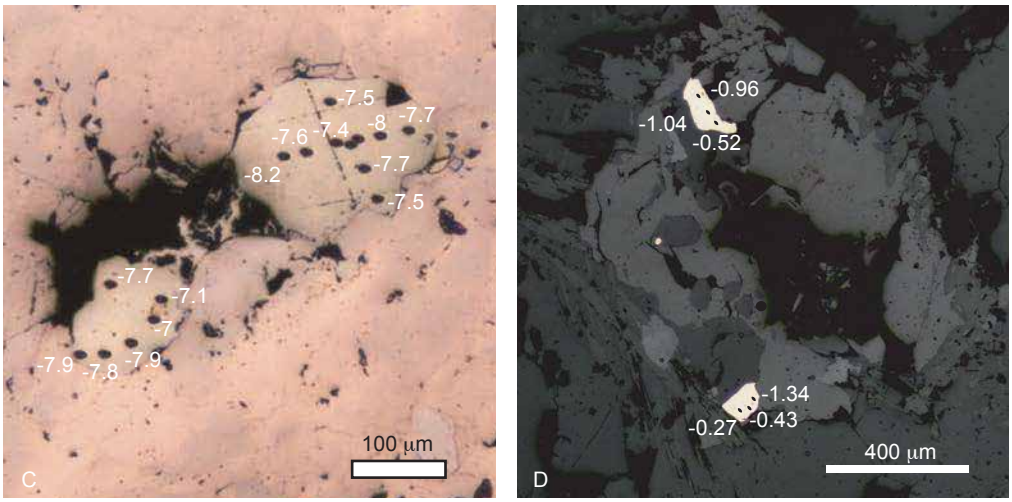
C
-7.5
-7.6
-7.4
-8
-7.7
-8.2
-7.7
-7.5
-7.7
-7.1
-7
-7.9
-7.8
-7.9
100 μm
D
-0.96
-1.04
-0.52
-1.34
-0.27
-0.43
400 μm

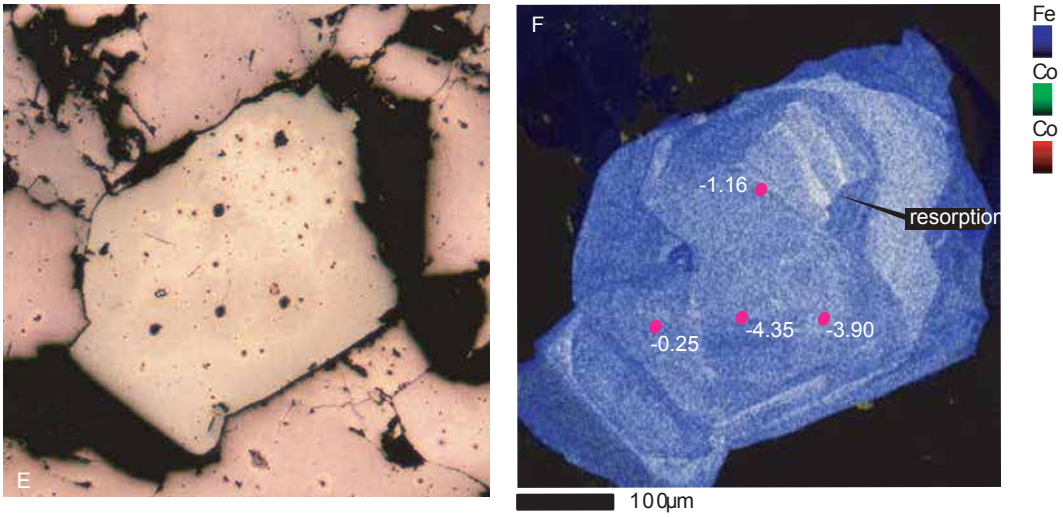
E
F
-1.16
resorption
-0.25
-4.35
-3.90
Fe
Co
Co
100μm

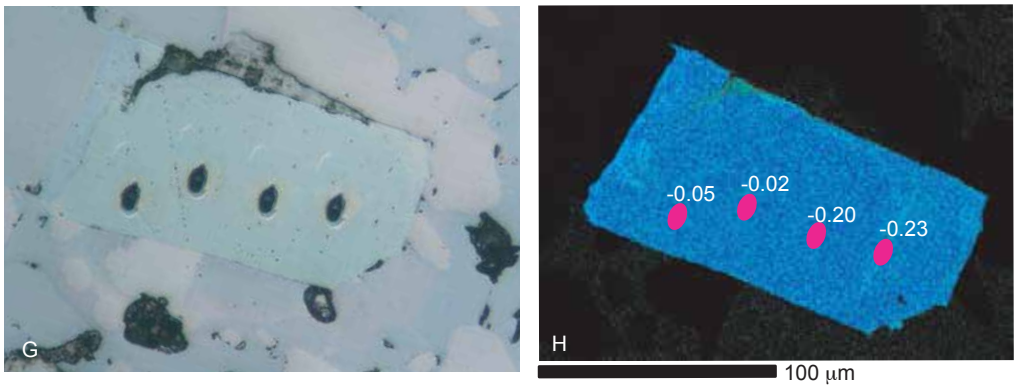
G
H
-0.05
-0.02
-0.20
-0.23
Fe
Co
100 μm

Figure 4

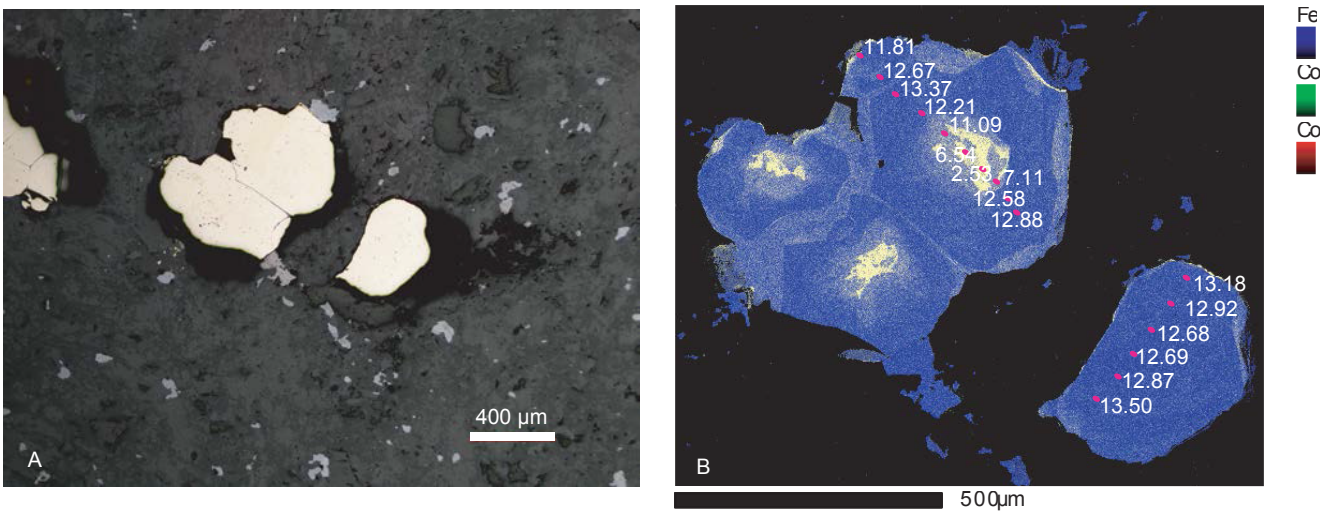
A
400 µm
B
500µm
11.81
12.67
13.37
12.21
11.09
7.11
12.58
12.88
13.18
12.92
12.68
12.69
12.87
13.50
Fe
Co
Co

Figure 5

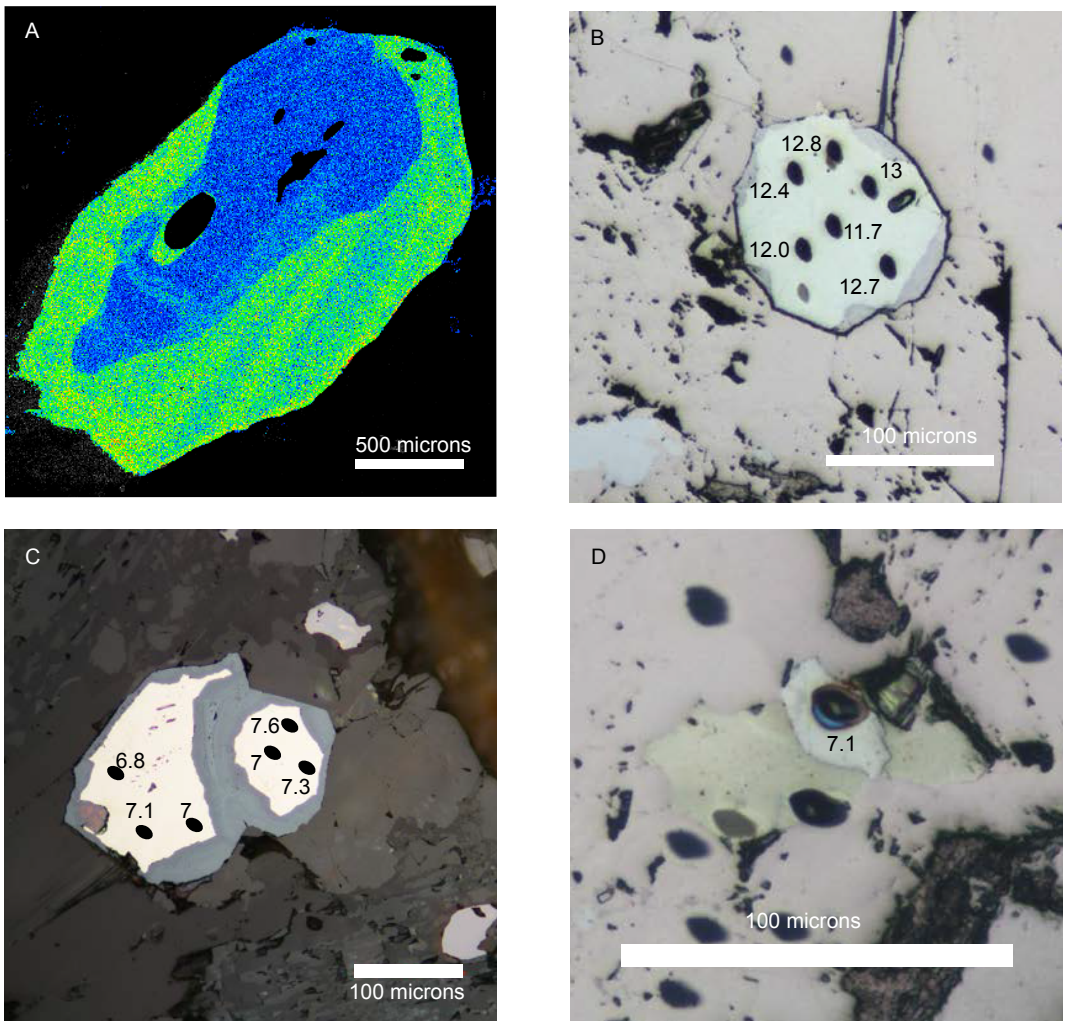
A
500 microns
B
12.8
13
12.4
11.7
12.0
12.7
100 microns
C
7.6
6.8
7
7.3
7.1
7
100 microns
D
7.1
100 microns

Figure 6

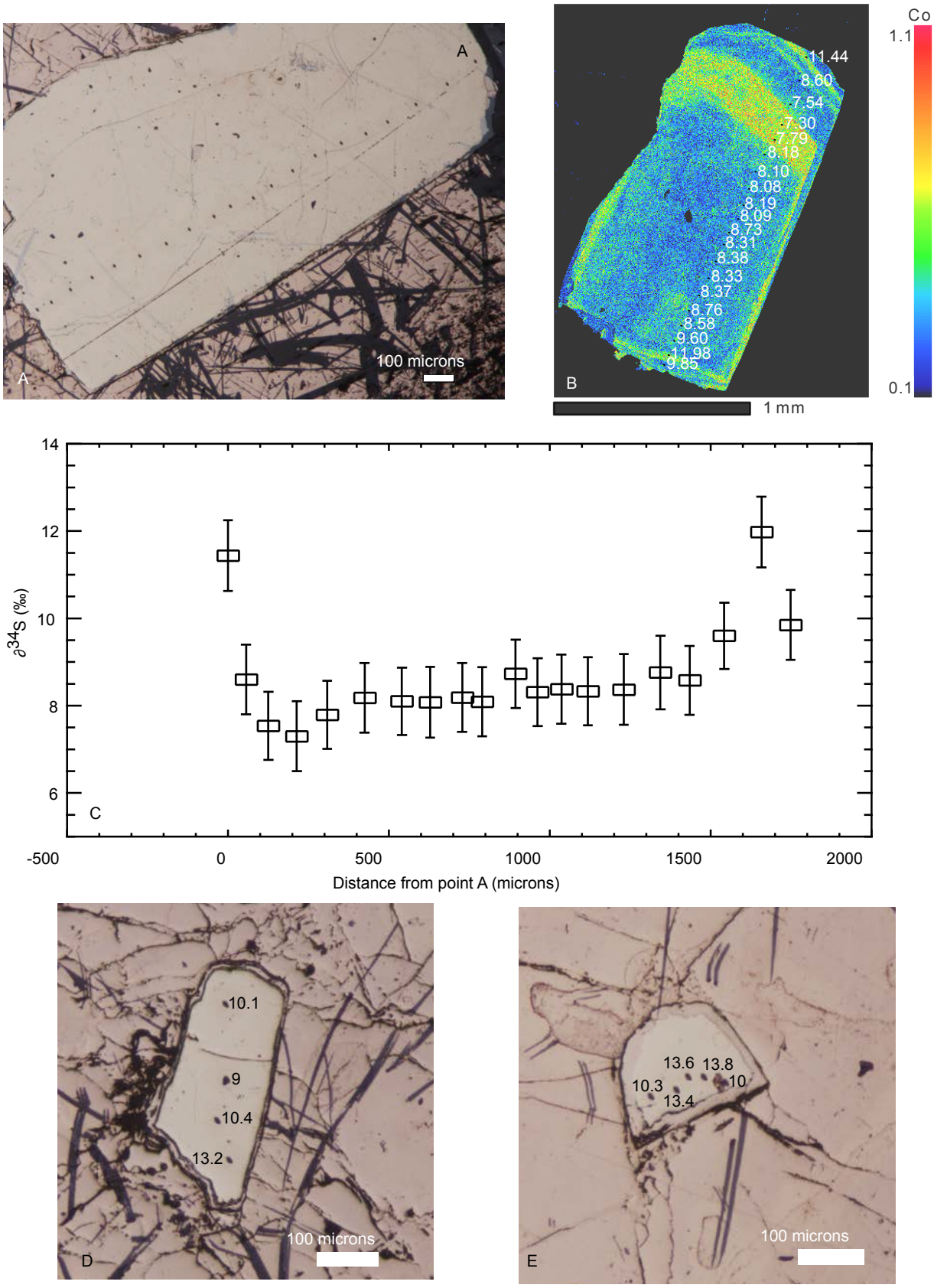
A
100 microns
A
B
11.44
8.60
7.54
7.30
7.79
8.18
8.10
8.08
8.19
8.09
8.73
8.31
8.38
8.33
8.37
8.76
8.58
9.60
11.98
9.85
1 mm
Co
1.1
0.1
14
12
10
8
6
$\partial^{34}S$ (‰)
C
-500
0
500
1000
1500
2000
Distance from point A (microns)
10.1
9
10.4
13.2
100 microns
D
13.6
13.8
10.3
10
13.4
100 microns
E

Figure 7

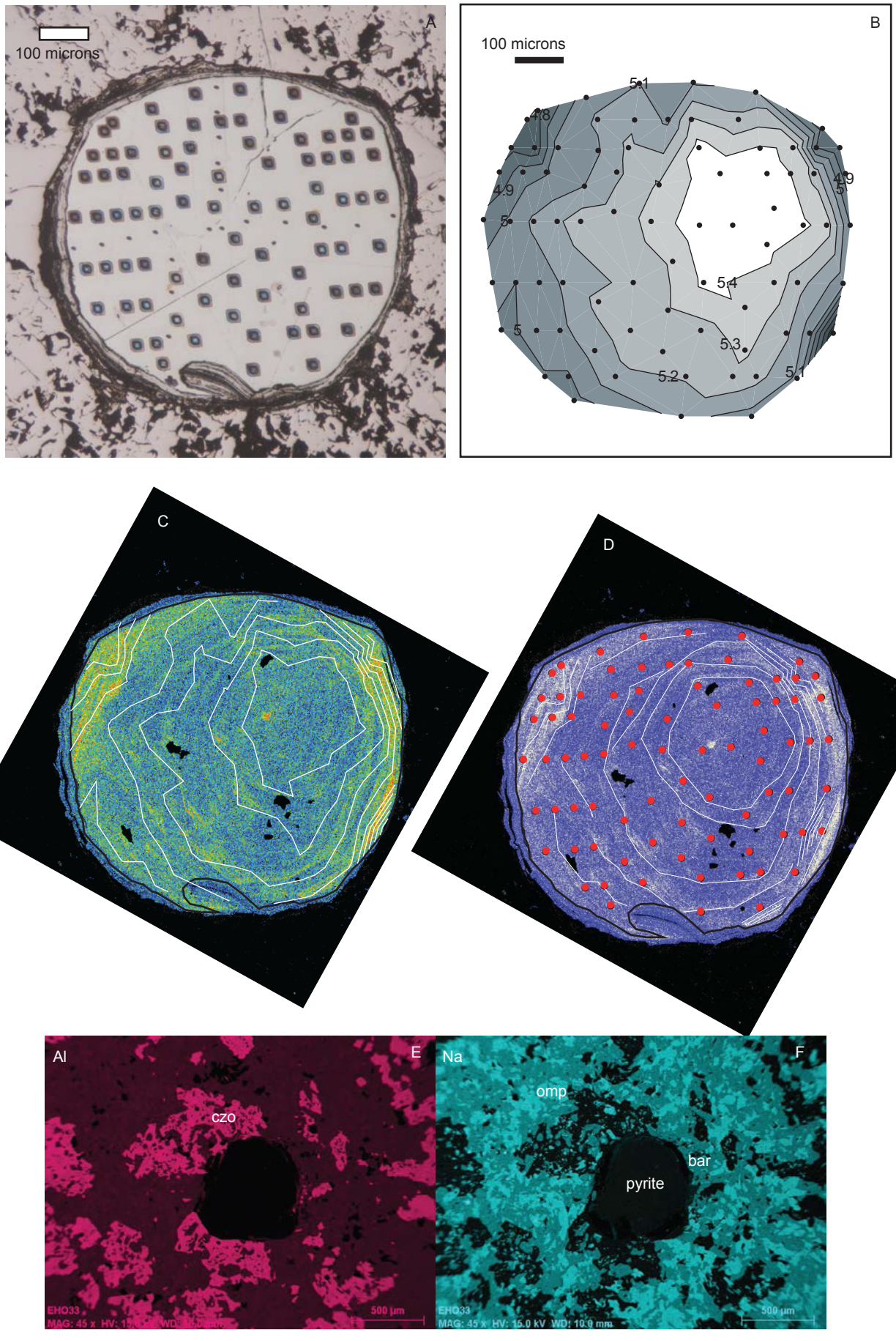
A
100 microns
B
100 microns
5.1
4.8
4.9
5
5.4
5.3
5.2
C
D
Al
E
czo
Na
F
omp
bar
pyrite

Figure 8

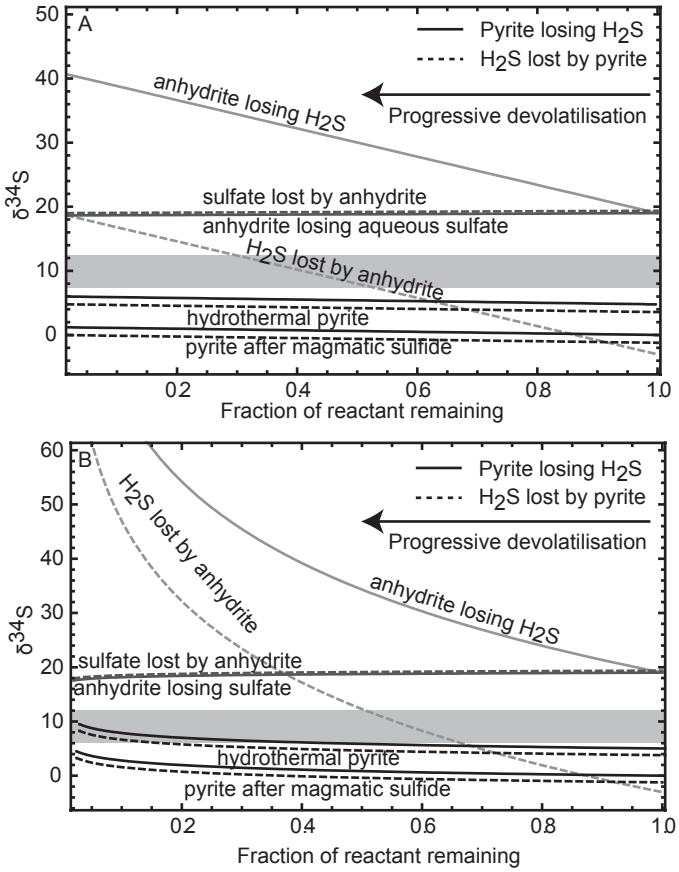
A
Pyrite losing H2S
H2S lost by pyrite
anhydrite losing H2S
Progressive devolatilisation
sulfate lost by anhydrite
anhydrite losing aqueous sulfate
H2S lost by anhydrite
hydrothermal pyrite
pyrite after magmatic sulfide
δ34S
Fraction of reactant remaining
B
Pyrite losing H2S
H2S lost by pyrite
Progressive devolatilisation
H2S lost by anhydrite
anhydrite losing H2S
sulfate lost by anhydrite
anhydrite losing sulfate
hydrothermal pyrite
pyrite after magmatic sulfide
δ34S
Fraction of reactant remaining

Figure 9

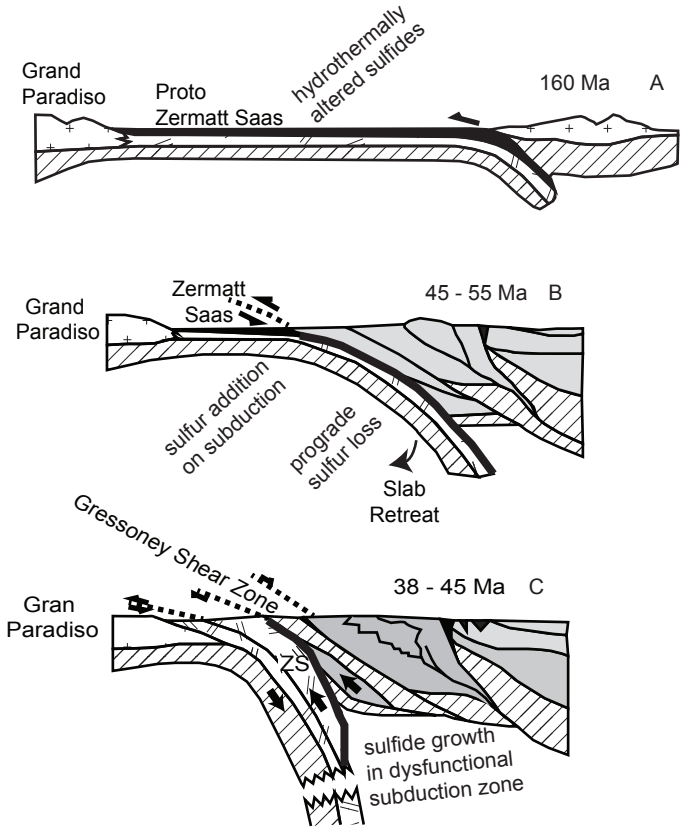
Grand
Paradiso
Proto
Zermatt Saas
hydrothermally
altered sulfides
160 Ma A
Zermatt
Saas
45 - 55 Ma B
Grand
Paradiso
sulfur addition
on subduction
prograde
sulfur loss
Slab
Retreat
Gressoney Shear Zone
38 - 45 Ma C
Gran
Paradiso
ZS
sulfide growth
in dysfunctional
subduction zone

Figure 10

Supplementary Tables

Supplementary Table 1a: LC004

Analysis	Phase	x	y	$\delta^{34}S_{VCDT}$ (‰)	1σ (‰)
Son3@02	pyrite standard	3587	2099	1.56	0.22
Son3@03	pyrite standard	3552	2099	1.68	0.23
Son3@04	pyrite standard	3517	2099	1.62	0.21
Son3@05	pyrite standard	3482	2099	1.66	0.20
Son3@06	pyrite standard	3447	2099	1.76	0.21
LC004_001@1	pyrite	-3333	1516	-6.43	0.17
LC004_001@2	pyrite	-3327	1492	-7.30	0.20
LC004_001@3	pyrite	-3376	1488	-5.77	0.15
LC004_002@1	pyrite	-4628	34	-6.93	0.20
LC004_002@02	pyrite	-4638	98	-7.12	0.19
LC004_002@03	pyrite	-4579	79	-7.60	0.20
LC004_002@04	pyrite	-4529	34	-10.06	0.20
LC004_002@05	pyrite	-4532	146	-7.77	0.20
LC004_002@06	pyrite	-4585	189	-8.35	0.22
LC004_002@07	pyrite	-4586	202	-8.02	0.20
LC004_002@08	pyrite	-4549	218	-8.14	0.21
LC004_002@09	pyrite	-4545	250	-8.31	0.19
LC004_002@10	pyrite	-4577	264	-7.59	0.19
LC004_002@11	pyrite	-4614	268	-7.55	0.20
LC004_002@12	pyrite	-4547	295	-7.12	0.21
Son3@07	pyrite standard	3412	2064	1.54	0.20
Son3@08	pyrite standard	3447	2064	1.55	0.21
Son3@09	pyrite standard	3482	2064	1.68	0.21
Son3@10	pyrite standard	3517	2064	1.58	0.22
LC004_002@13	pyrite	-4581	332	-6.88	0.19
LC004_003@1	pyrite	-7057	2444	-6.69	0.20
LC004_003@2	pyrite	-7077	2454	-6.67	0.20
LC004_004@1	pyrite	1586	4778	-7.70	0.21
LC004_004@02	pyrite	1618	4778	-7.69	0.20
LC004_004@03	pyrite	1643	4777	-7.95	0.21
LC004_004@04	pyrite	1667	4777	-7.41	0.20
LC004_004@05	pyrite	1702	4781	-7.56	0.21
LC004_004@06	pyrite	1727	4781	-8.15	0.20
LC004_004@08	pyrite	1641	4809	-7.50	0.21
LC004_004@09	pyrite	1651	4782	-7.95	0.22
LC004_004@10	pyrite	1665	4732	-7.50	0.20
LC004_004@11	pyrite	1942	4880	-7.71	0.19
LC004_004@12	pyrite	1989	4948	-7.88	0.19
LC004_004@13	pyrite	1962	4952	-7.82	0.20
LC004_004@14	pyrite	1930	4946	-7.90	0.19

LC004_004@15	pyrite	1900	4926	-6.96	0.20
LC004_004@16	pyrite	1887	4906	-7.08	0.21
LC004_005@1	pyrite	2071	-1870	-8.36	0.20
Son3@11	pyrite standard	3552	2064	1.33	0.24
Son3@12	pyrite standard	3587	2064	1.70	0.22
Son3@13	pyrite standard	3622	2064	1.73	0.23
Son3@14	pyrite standard	3657	2064	1.39	0.21
LC004_005@2	pyrite	2071	-1870	-11.54	0.19
LC004_005@03	pyrite	2084	-1837	-7.10	0.21
LC004_005@04	pyrite	2094	-1794	-7.24	0.22
LC004_005@05	pyrite	2033	-1746	-7.05	0.20
LC004_005@06	pyrite	1997	-1732	-6.97	0.22
LC004_005@07	pyrite	1936	-1764	-9.25	0.20
LC004_005@08	chalcopyrite	2131	-1750	-12.09	0.36
LC004_005@09	chalcopyrite	2132	-1750	-16.90	0.20
LC004_005@10	chalcopyrite	2117	-1709	-12.16	0.35
LC004_005@11	pyrrhotite	2054	-1667	-12.63	0.34
LC004_005@12	pyrrhotite	2117	-1644	-14.65	0.29
SON3@15	pyrite standard	3824	2140	1.62	0.20
SON3@16	pyrite standard	3859	2140	1.46	0.20
SON3@17	pyrite standard	3894	2140	1.73	0.22
SON3@18	pyrite standard	3929	2140	2.08	0.22

Supplementary Table 1b: LC008AA

Analysis	Phase	x	y	$\delta^{34}S_{VCDT}$ (‰)	1σ (‰)
Son3@2	pyrite standard	5168	-2144	1.71	0.39
Son3@3	pyrite standard	5130	-2137	1.73	0.39
Son3@4	pyrite standard	5092	-2140	1.70	0.39
Son3@5	pyrite standard	5059	-2170	1.60	0.38
LC008A-082@1	pyrite	-6352	3108	-4.26	0.38
LC008A-082@2	pyrite	-6273	3254	-2.02	0.39
LC008A-082@3	pyrite	-6213	3131	-4.19	0.37
LC008A-082@4	pyrite	-6175	3077	-4.36	0.36
LC008A-082@5	pyrite	-6386	3197	-6.70	0.37
LC008A-0003@1	pyrite	-3380	3535	-3.88	0.38
LC008A-0003@2	pyrite	-3375	3622	-4.33	0.39
LC008A-0003@3	pyrite	-3245	3597	-1.14	0.37
LC008A-0003@4	pyrite	-3382	3712	-0.22	0.38
LC008A-0006@1	pyrite	2353	4109	3.73	0.37
LC008A-0006@2	pyrite	2323	4128	-0.27	0.47
LC008A-0006@3	pyrite	2290	4158	-2.96	0.38
LC008A-0006@4	pyrite	2259	4211	-2.60	0.36
Son3@6	pyrite standard	5045	-2133	1.62	0.38
Son3@7	pyrite standard	4988	-2147	1.65	0.38
Son3@8	pyrite standard	4946	-2143	1.72	0.39
Son3@9	pyrite standard	5046	-2174	1.50	0.41
Son3@11	pyrite standard	5098	-2161	1.39	0.39
Son3@12	pyrite standard	5031	-2153	1.57	0.40
Son3@13	pyrite standard	4909	-2147	1.58	0.40
Son3@14	pyrite standard	4885	-2148	1.66	0.40
LC008A-0007@1	pyrite	4644	4598	0.68	0.36
LC008A-0007@2	pyrite	4619	4545	-0.41	0.35
LC008A-0007@3	pyrite	4585	4505	-0.95	0.36
LC008A-0007@4	pyrite	4555	4484	1.09	0.37
LC008A-0007@5	pyrite	4578	4375	3.94	0.37
LC008A-0004@1	pyrite	-3743	4733	0.26	0.38
LC008A-0004@2	pyrite	-3786	4736	1.09	0.38
LC008A-0004@3	pyrite	-3781	4788	-0.75	0.34
LC008A-0004@4	pyrite	-3800	4795	-0.57	0.38
LC008A-0004@5	pyrite	-3780	4850	-0.63	0.37
LC008A-0003b@1	pyrite	-4042	4154	0.73	0.37
LC008A-0008@1	pyrite	-4721	5696	0.57	0.37
LC008A-0008@2	pyrite	-4919	5803	-1.03	0.36
LC008A-0008@3	pyrite	-5474	6180	2.42	0.37
LC008A-0008@4	pyrite	-5556	6415	-2.28	0.34

LC008A-0008@5	pyrite	-5238	6030	-2.06	0.34
LC008A-0008@6	pyrite	-4046	4170	-4.66	0.39
Son3@15	pyrite standard	4851	-2144	1.75	0.39
Son3@16	pyrite standard	5542	-1247	1.58	0.37
Son3@17	pyrite standard	5511	-1237	1.80	0.39
Son3@18	pyrite standard	5480	-1248	1.62	0.41
Son3@20	pyrite standard	5519	-1197	1.66	0.30
Son3@21	pyrite standard	5488	-1207	1.77	0.29
Son3@22	pyrite standard	5454	-1227	1.53	0.30
Son3@23	pyrite standard	5445	-1187	1.99	0.28
LC008A-0005@1	pyrite	-1806	4557	-0.22	0.24
LC008A-0005@2	pyrite	-1828	4551	-0.39	0.27
LC008A-0005@3	pyrite	-1842	4530	-1.32	0.21
LC008A-0005@4	pyrite	-1739	3845	-0.95	0.27
LC008A-0005@5	pyrite	-1760	3881	-1.04	0.26
LC008A-0005@6	pyrite	-1776	3904	-0.53	0.25
LC008A-0008b@1	pyrite	-5372	5235	-4.13	0.22
LC008A-0008b@2	pyrite	-5400	5251	-0.98	0.20
LC008A-0008b@3	pyrite	-5410	5279	-0.96	0.19
LC008A-001@1	pyrite	-4278	-1230	-0.12	0.24
LC008A-001@2	pyrite	-4270	-1202	-0.09	0.24
LC008A-001@3	pyrite	-4257	-1174	-0.29	0.25
LC008A-001@4	pyrite	-4260	-1145	-0.33	0.24
Son3@24	pyrite standard	5481	-1186	1.42	0.27
Son3@25	pyrite standard	5522	-1181	1.41	0.28
Son3@26	pyrite standard	5591	-1198	1.36	0.26
Son3@27	pyrite standard	5079	-2138	1.76	0.28
Son3@28	pyrite standard	5016	-2120	1.41	0.27

Supplementary Table 1c: PF005

Analysis	Phase	x	y	$\delta^{34}S_{VCDT}$ (‰)	1σ (‰)
Son3@02	pyrite standard	3852	288	1.55	0.25
Son3@03	pyrite standard	3791	305	1.35	0.25
Son3@04	pyrite standard	3752	273	2.21	0.25
Son3@05	pyrite standard	3712	264	2.47	0.26
PF005_0015@1	pyrite	-2560	-1604	16.17	0.24
PF005_0015@2	pyrite	-2610	-1604	14.70	0.31
PF005_0015@3	pyrite	-2670	-1604	12.64	0.26
PF005_0015@4	pyrite	-2730	-1604	14.11	0.25
PF005_0015@5	pyrite	-2845	-1624	11.38	0.31
PF005_0015@6	pyrite	-2899	-1641	12.17	0.28
PF005_0015@7	pyrite	-2919	-1664	14.82	0.26
PF005_0015@8	pyrite	-2959	-1583	12.56	0.32
PF005_0015@9	pyrite	-2983	-1508	12.75	0.28
PF005_0015@10	pyrite	-3044	-1447	10.87	0.26
PF005_0017@1	pyrite	1510	3762	5.28	0.28
PF005_0017@2	pyrite	1522	3822	10.23	0.33
PF005_0017@3	pyrite	1532	3869	13.30	0.28
Son3@06	pyrite standard	3712	290	1.82	0.24
Son3@07	pyrite standard	3712	314	1.31	0.27
Son3@08	pyrite standard	3624	320	1.39	0.24
Son3@09	pyrite standard	3630	286	1.65	0.25
PF005_0017@4	pyrite	1580	3934	15.45	0.29
PF005_0017@5	pyrite	1623	3988	10.13	0.30
PF005_0017@6	pyrite	1643	4034	11.24	0.28
PF005_0017@7	pyrite	1602	4075	15.51	0.25
PF005_0017@8	pyrite	1552	4102	12.02	0.26
PF005_0017@9	pyrite	1508	4118	12.55	0.26
PF005_0017@10	pyrite	1372	4164	12.46	0.24
PF005_0019@1	pyrite	4266	6799	3.35	0.24
PF005_0019@2	pyrite	4286	6880	3.01	0.27
PF005_0019@3	pyrite	3914	7160	10.44	0.21
PF005_0019@4	pyrite	3870	7205	12.17	0.26
Son3@10	pyrite standard	3587	314	1.31	0.26
Son3@11	pyrite standard	3568	284	1.83	0.26
Son3@12	pyrite standard	3570	318	1.12	0.25
Son3@13	pyrite standard	3554	282	1.76	0.26
Son3@14	pyrite standard	3533	336	1.20	0.26
PF005_0019@5	pyrite	3831	7241	12.44	0.26
PF005_0019@6	pyrite	3783	7276	12.51	0.23
PF005_0019@7	pyrite	3743	7323	11.84	0.27
PF005_0019@8	pyrite	3700	7349	11.62	0.26

PF005_0019@9	pyrite	3645	7364	11.32	0.31
PF005_0020@1	pyrite	2748	7382	11.84	0.25
PF005_0020@2	pyrite	2718	7428	12.70	0.27
PF005_0020@3	pyrite	2696	7466	13.39	0.28
PF005_0020@4	pyrite	2655	7510	12.24	0.27
PF005_0020@5	pyrite	2620	7555	11.12	0.28
PF005_0020@6	pyrite	2588	7597	6.55	0.28
PF005_0020@7	pyrite	2563	7634	2.54	0.29
PF005_0020@8	pyrite	2543	7661	7.13	0.26
PF005_0020@9	pyrite	2528	7697	12.60	0.27
PF005_0020@10	pyrite	2516	7725	12.90	0.28
Son3@15	pyrite standard	3449	303	1.90	0.29
Son3@16	pyrite standard	3443	326	0.98	0.28
Son3@17	pyrite standard	4256	533	1.58	0.28
Son3@18	pyrite standard	4230	550	1.51	0.27
Son3@19	pyrite standard	4201	566	1.92	0.26
PF005_0020B@1	pyrite	2232	7898	13.53	0.27
PF005_0020B@2	pyrite	2269	7939	12.90	0.26
PF005_0020B@3	pyrite	2313	7979	12.71	0.28
PF005_0020B@4	pyrite	2353	8016	12.70	0.27
PF005_0020B@5	pyrite	2389	8051	12.94	0.28
PF005_0020B@6	pyrite	2436	8083	13.20	0.27
PF005_0022@1	pyrite	3292	-2775	13.60	0.29
PF005_0022@2	pyrite	3316	-2747	13.35	0.31
PF005_0022@3	pyrite	3338	-2695	14.39	0.28
PF005_0022@4	pyrite	3364	-2638	2.51	0.28
PF005_0022@5	pyrite	3375	-2592	12.35	0.29
PF005_0022@6	pyrite	3416	-2554	6.36	0.28
PF005_0022@7	pyrite	3481	-2514	12.53	0.26
Son3@20	pyrite standard	4172	580	1.85	0.28
Son3@21	pyrite standard	4201	588	1.87	0.29
Son3@22	pyrite standard	4230	571	1.78	0.27
Son3@23	pyrite standard	4263	548	1.61	0.29
PF005_0022@8	pyrite	3509	-2481	10.62	0.28
PF005_0022@9	pyrite	3549	-2444	10.00	0.28
PF005_0022@10	pyrite	3576	-2396	11.14	0.28
PF005_0022@11	pyrite	3574	-2338	11.95	0.27
PF005_0022@12	pyrite	3568	-2276	13.02	0.29
PF005_0022@13	pyrite	3595	-2237	11.75	0.28
PF005_0018@1	pyrite	1131	2276	3.73	0.32
Son3@24	pyrite standard	4295	562	1.34	0.28
Son3@25	pyrite standard	4275	582	1.79	0.29
Son3@26	pyrite standard	4313	597	1.73	0.28

Son3@27	pyrite standard	4343	618	1.37	0.29

Supplementary Table 1d: PF008

Analysis	Phase	x	y	$\delta^{34}S_{VCDT}$ (‰)	1σ (‰)
Son3@1	pyrite standard	5286	1787	1.46	0.25
Son3@02	pyrite standard	5251	1787	1.55	0.24
Son3@03	pyrite standard	5216	1787	1.75	0.25
Son3@04	pyrite standard	5181	1787	1.68	0.26
Son3@05	pyrite standard	5146	1787	1.69	0.25
Son3@06	pyrite standard	5111	1787	1.64	0.24
PF008_0024@1	pyrite	-6004	-4332	7.31	0.21
PF008_0024@02	pyrite	-5992	-4302	13.13	0.22
PF008_0024@03	pyrite	-5973	-4265	12.81	0.21
PF008_0024@04	pyrite	-5966	-4228	6.04	0.20
PF008_0024@05	pyrite	-5948	-4197	6.07	0.20
PF008_0024@06	pyrite	-5931	-4168	5.91	0.20
PF008_0024@07	pyrite	-5924	-4134	5.96	0.21
PF008_0024@08	pyrite	-5922	-4098	6.03	0.20
PF008_0024@09	pyrite	-5913	-4067	6.07	0.21
PF008_0024@10	pyrite	-5880	-4045	5.91	0.21
PF008_0024@11	pyrite	-5813	-4064	4.99	0.20
PF008_0024@12	pyrite	-5789	-4094	10.69	0.21
Son3@07	pyrite standard	5076	1787	1.38	0.24
Son3@08	pyrite standard	5041	1787	1.58	0.23
Son3@09	pyrite standard	5006	1787	1.79	0.23
Son3@10	pyrite standard	4971	1787	1.66	0.22
Son3@11	pyrite standard	4936	1787	1.85	0.24
PF008-0027@1	pyrite	505	5439	12.87	0.22
PF008-0027@2	pyrite	476	5436	13.02	0.22
PF008-0027@3	pyrite	511	5466	12.46	0.23
PF008-0027@4	pyrite	472	5492	11.98	0.21
PF008-0027@5	pyrite	432	5458	12.74	0.22
PF008-0027@6	pyrite	472	5468	11.67	0.19
PF008-0026@1	pyrite	2106	7169	5.26	0.23
PF008-0026@2	pyrite	2100	7149	7.86	0.17
PF008-0026@3	pyrite	2076	7159	10.91	0.26
PF008-0032@1	pyrite	3758	-200	7.05	0.22
PF008-0032@2	pyrite	3801	-179	7.07	0.23
PF008-0032@3	pyrite	3846	-218	6.82	0.18
PF008-0032@4	pyrite	3712	-315	7.60	0.24
PF008-0032@5	pyrite	3715	-286	6.98	0.21
PF008-0032@6	pyrite	3679	-282	7.34	0.22
Son3@12	pyrite standard	4971	1822	2.01	0.21
Son3@13	pyrite standard	5006	1822	1.80	0.22
Son3@14	pyrite standard	5041	1822	1.84	0.23

Son3@15	pyrite standard	5076	1822	1.52	0.22
PF008-0031@1	pyrite	2595	-1159	6.88	0.22
Son3@16	pyrite standard	5111	1822	1.32	0.23
Son3@17	pyrite standard	5146	1822	1.31	0.22
PF008-0024@14	pyrite	-5969	-4368	10.58	0.16
PF008-0024@15	pyrite	-5938	-4363	12.80	0.20
PF008-0024@16	pyrite	-5840	-4256	12.71	0.19
PF008-0024@17	pyrite	-5888	-4222	13.07	0.20
PF008-0024@18	pyrite	-5916	-4209	8.12	0.22
PF008-0024@19	pyrite	-5973	-4179	5.99	0.24
PF008_0024_chalc@1	chalcopyrite	-5715	-4254	0.52	0.17
PF008_0028@1	chalcopyrite	-3568	5144	12.50	0.21
PF008_0028@2	pyrite	-3563	5172	7.10	0.30
Son3@18	pyrite standard	5181	1822	1.45	0.23
Son3@19	pyrite standard	5216	1822	1.41	0.23
Son3@20	pyrite standard	5251	1822	1.53	0.23
Son3@21	pyrite standard	5286	1822	1.57	0.23

Supplementary Table 1e: ATPF004

Analysis	Phase	x	y	$\delta^{34}S_{VCDT}$ (‰)	1σ (‰)
Son3@02	pyrite standard	-4481	1733	1.86	0.35
Son3@03	pyrite standard	-4511	1733	1.88	0.36
Son3@04	pyrite standard	-4541	1733	1.61	0.38
Son3@05	pyrite standard	-4571	1733	1.78	0.36
ATPF004_G1@1	pyrite	805	856	11.46	0.34
ATPF004_G1@2	pyrite	776	810	8.62	0.34
ATPF004_G1@3	pyrite	741	740	7.56	0.33
ATPF004_G1@4	pyrite	697	666	7.32	0.34
ATPF004_G1@5	pyrite	650	592	7.81	0.32
ATPF004_G1@6	pyrite	592	517	8.19	0.34
ATPF004_G1@7	pyrite	534	432	8.11	0.31
ATPF004_G1@8	pyrite	490	350	8.10	0.34
ATPF004_G1@9	pyrite	440	269	8.21	0.32
ATPF004_G1@10	pyrite	409	209	8.11	0.32
Son3@06	pyrite standard	-4601	1733	1.16	0.31
Son3@07	pyrite standard	-4631	1733	1.39	0.34
Son3@08	pyrite standard	-4661	1733	1.45	0.32
Son3@09	pyrite standard	-4691	1733	1.39	0.32
ATPF004_G1@11	pyrite	357	144	8.76	0.31
ATPF004_G1@12	pyrite	323	77	8.33	0.31
ATPF004_G1@13	pyrite	286	-2	8.40	0.31
ATPF004_G1@14	pyrite	245	-84	8.35	0.31
ATPF004_G1@15	pyrite	189	-165	8.40	0.33
ATPF004_G1@16	pyrite	132	-235	8.78	0.34
ATPF004_G1@17	pyrite	87	-307	8.60	0.31
ATPF004_G1@18	pyrite	33	-409	9.62	0.29
ATPF004_G1@19	pyrite	-25	-526	12.01	0.32
ATPF004_G1@20	pyrite	-70	-643	9.88	0.31
Son3@10	pyrite standard	-4721	1733	1.27	0.28
Son3@11	pyrite standard	-4721	1763	1.93	0.29
Son3@12	pyrite standard	-4691	1763	1.63	0.30
Son3@13	pyrite standard	-4661	1763	1.95	0.33
ATPF004_G2@1	pyrite	-2969	-681	13.24	0.33
ATPF004_G2@2	pyrite	-3000	-652	12.36	0.33
ATPF004_G2@3	pyrite	-3045	-616	12.36	0.35
ATPF004_G2@4	pyrite	-3014	-427	11.96	0.33
ATPF004_G2@5	pyrite	-2871	-530	12.69	0.32
ATPF004_G2@6	pyrite	-2908	-579	12.93	0.33
ATPF004_G2@7	pyrite	-2912	-532	12.60	0.29
ATPF004_G2@8	pyrite	-2933	-567	12.48	0.31

ATPF004_G3@1	pyrite	-2390	2934	10.03	0.30
ATPF004_G3@2	pyrite	-2356	2944	13.81	0.29
ATPF004_G3@3	pyrite	-2334	2956	13.61	0.28
ATPF004_G3@4	pyrite	-2329	2983	13.39	0.32
ATPF004_G3@5	pyrite	-2299	3012	10.31	0.30
ATPF004_G4@1	pyrite	2089	614	9.61	0.31
ATPF004_G4@2	pyrite	2055	662	8.74	0.33
Son3@14	pyrite standard	-4631	1763	1.89	0.31
Son3@15	pyrite standard	-4601	1763	1.61	0.31
ATPF004_G4@3	pyrite	2028	702	9.02	0.31
ATPF004_G4@4	pyrite	1986	747	8.39	0.31
ATPF004_G4@5	pyrite	1924	808	10.05	0.32
ATPF004_G5@1	pyrite	2944	-614	10.16	0.33
ATPF004_G5@2	pyrite	2878	-502	9.05	0.32
ATPF004_G5@3	pyrite	2858	-431	10.39	0.32
ATPF004_G5@4	pyrite	2806	-382	13.22	0.33
Son3@16	pyrite standard	-4571	1763	1.55	0.32

Supplementary Table 1f: EH033 standard analyses

Analysis	Phase	x	y	$\delta^{34}S_{VCDT}$ (‰)	1σ (‰)
Son3@02	pyrite standard	3431	1138	2.22	0.29
Son3@03	pyrite standard	3401	1138	1.45	0.28
Son3@04	pyrite standard	3371	1138	1.47	0.29
Son3@05	pyrite standard	3341	1138	1.77	0.29
EH033_G1x@1	pyrite	1998	-1246	5.06	0.29
EH033_G1x@2	pyrite	2003	-1144	5.21	0.30
EH033_G1x@3	pyrite	2020	-1034	5.27	0.27
EH033_G1x@4	pyrite	2028	-953	5.30	0.31
EH033_G1x@6	pyrite	2167	-786	5.82	0.29
EH033_G1x@7	pyrite	2164	-717	5.47	0.29
EH033_G1x@8	pyrite	2173	-651	5.42	0.30
EH033_G1x@9	pyrite	2173	-587	5.26	0.29
EH033_G1x@10	pyrite	2177	-523	5.15	0.27
EH033_G1y@1	pyrite	2595	-889	4.84	0.29
EH033_G1y@2	pyrite	2501	-906	5.46	0.31
EH033_G1y@3	pyrite	2416	-903	5.62	0.30
EH033_G1y@4	pyrite	2320	-883	5.67	0.31
EH033_G1y@5	pyrite	2223	-873	5.64	0.28
EH033_G1y@6	pyrite	2159	-885	5.14	0.29
EH033_G1y@7	pyrite	1990	-881	5.49	0.27
EH033_G1y@8	pyrite	1922	-891	5.48	0.29
Son3@06	pyrite standard	3311	1138	1.79	0.31
Son3@07	pyrite standard	3281	1138	1.75	0.30
Son3@08	pyrite standard	3251	1138	1.70	0.28
Son3@09	pyrite standard	3221	1138	1.63	0.29
EH033_G1y@9	pyrite	1852	-901	5.02	0.31
EH033_G1y@10	pyrite	1779	-905	5.26	0.29
EH033_G2@1	pyrite	-1448	-122	5.62	0.30
EH033_G2@2	pyrite	-1526	-123	5.73	0.29
EH033_G2@3	pyrite	-1596	-137	5.57	0.27
EH033_G2@4	pyrite	-1655	-140	5.88	0.29
EH033_G2@5	pyrite	-1720	-148	5.96	0.28
EH033_G2@6	pyrite	-1774	-160	6.17	0.30
EH033_G2@7	pyrite	-1869	-167	6.28	0.28
EH033_G2@8	pyrite	-1958	-178	5.93	0.29
EH033_G2@9	pyrite	-2031	-195	4.40	0.28
EH033_G2@10	pyrite	-2101	-212	0.86	0.29
Son3@10	pyrite standard	3161	1168	1.52	0.30
Son3@11	pyrite standard	3191	1168	1.69	0.34
Son3@12	pyrite standard	3221	1168	1.81	0.28
Son3@13	pyrite standard	3251	1168	1.38	0.30

EH033_G2@12	pyrite	-2185	-217	0.99	0.28
EH033_G2@13	pyrite	-2219	-229	-1.06	0.26
Son3@14	pyrite standard	3281	1168	1.62	0.30
Son3@15	pyrite standard	3311	1168	1.71	0.31
Son3@16	pyrite standard	3341	1168	1.46	0.30
Son3@17	pyrite standard	3371	1168	1.57	0.30
Son3@18	pyrite standard	3401	1168	1.45	0.31

Supplementary Table 1g: EH033 high precision analyses

Analysis	Phase	x	y	$\delta^{34}S_{VCDT}$ (‰)	1σ (‰)
Son3@02	pyrite standard	3448	1210	1.80	0.06
Son3@03	pyrite standard	3378	1210	1.60	0.06
Son3@04	pyrite standard	3308	1210	1.74	0.06
Son3@05	pyrite standard	3238	1210	1.68	0.06
EH033_hp@1	pyrite	2368	-1238	5.11	0.06
EH033_hp@2	pyrite	2218	-1238	5.18	0.06
EH033_hp@3	pyrite	1990	-1204	5.02	0.06
EH033_hp@4	pyrite	1928	-1153	5.03	0.06
EH033_hp@5	pyrite	1978	-1153	5.03	0.06
EH033_hp@6	pyrite	2078	-1153	5.21	0.06
EH033_hp@7	pyrite	2228	-1153	5.26	0.05
EH033_hp@8	pyrite	2328	-1153	5.32	0.05
EH033_hp@9	pyrite	2378	-1153	5.29	0.05
EH033_hp@10	pyrite	2465	-1157	5.13	0.05
Son3@06	pyrite standard	3168	1210	1.76	0.05
Son3@07	pyrite standard	3098	1210	1.77	0.05
Son3@08	pyrite standard	3098	1280	1.84	0.05
Son3@09	pyrite standard	3168	1280	1.67	0.05
EH033_hp@11	pyrite	2542	-1061	4.54	0.05
EH033_hp@12	pyrite	2492	-1061	5.10	0.05
EH033_hp@13	pyrite	2442	-1061	5.27	0.05
EH033_hp@14	pyrite	2260	-1055	5.31	0.05
EH033_hp@15	pyrite	2110	-1055	5.31	0.05
EH033_hp@16	pyrite	1960	-1055	5.12	0.05
EH033_hp@17	pyrite	1910	-1055	5.11	0.05
EH033_hp@18	pyrite	1835	-1054	5.00	0.05
EH033_hp@19	pyrite	1816	-953	5.12	0.05
EH033_hp@20	pyrite	1866	-953	5.05	0.05
Son3@10	pyrite standard	3238	1280	1.73	0.05
Son3@11	pyrite standard	3308	1280	1.69	0.05
Son3@12	pyrite standard	3378	1280	1.55	0.05
Son3@13	pyrite standard	3448	1280	1.75	0.04
EH033_hp@21	pyrite	1916	-953	5.10	0.04
EH033_hp@22	pyrite	1966	-953	5.16	0.04
EH033_hp@23	pyrite	2116	-953	5.29	0.04
EH033_hp@24	pyrite	2266	-953	5.46	0.04
EH033_hp@25	pyrite	2416	-953	5.41	0.04
EH033_hp@26	pyrite	2466	-953	5.29	0.04
EH033_hp@27	pyrite	2563	-955	5.09	0.04
EH033_hp@28	pyrite	2578	-831	5.04	0.04
EH033_hp@29	pyrite	2528	-831	5.41	0.04

EH033_hp@30	pyrite	2478	-831	5.47	0.04
EH033_hp@31	pyrite	2328	-831	5.55	0.04
EH033_hp@32	pyrite	2154	-823	5.38	0.04
EH033_hp@33	pyrite	2004	-823	5.31	0.04
EH033_hp@34	pyrite	1954	-823	5.22	0.04
EH033_hp@35	pyrite	1904	-823	5.17	0.04
EH033_hp@36	pyrite	1797	-819	4.98	0.04
EH033_hp@37	pyrite	1854	-823	5.06	0.04
Son3@14	pyrite standard	3518	1280	1.46	0.04
Son3@15	pyrite standard	3459	1112	1.14	0.04
Son3@16	pyrite standard	3389	1112	1.48	0.04
Son3@17	pyrite standard	3319	1112	1.61	0.04
EH033_hp@38	pyrite	1831	-718	4.88	0.04
EH033_hp@39	pyrite	1881	-718	4.99	0.04
EH033_hp@40	pyrite	1931	-718	5.04	0.04
EH033_hp@41	pyrite	2081	-718	5.23	0.04
EH033_hp@42	pyrite	2301	-721	5.53	0.04
EH033_hp@43	pyrite	2401	-721	5.45	0.04
EH033_hp@44	pyrite	2451	-721	5.45	0.04
EH033_hp@45	pyrite	2501	-721	5.31	0.04
EH033_hp@46	pyrite	2568	-721	4.89	0.04
EH033_hp@47	pyrite	2556	-666	4.84	0.04
EH033_hp@48	pyrite	2506	-666	4.95	0.04
EH033_hp@49	pyrite	2456	-666	5.44	0.04
EH033_hp@50	pyrite	2256	-666	5.49	0.04
EH033_hp@51	pyrite	2106	-666	5.27	0.04
EH033_hp@52	pyrite	1956	-666	5.10	0.04
Son3@18	pyrite standard	3249	1112	1.61	0.04
Son3@19	pyrite standard	3179	1112	1.72	0.04
Son3@20	pyrite standard	3179	1112	1.53	0.04
Son3@21	pyrite standard	3129	1140	1.58	0.04
EH033_hp@53	pyrite	1890	-606	4.77	0.04
EH033_hp@54	pyrite	2040	-606	5.16	0.04
EH033_hp@55	pyrite	1906	-666	4.76	0.04
EH033_hp@56	pyrite	1856	-666	4.82	0.04
EH033_hp@57	pyrite	2190	-606	5.13	0.04
EH033_hp@58	pyrite	2240	-606	5.35	0.04
EH033_hp@59	pyrite	2340	-606	5.28	0.04
EH033_hp@60	pyrite	2519	-625	4.91	0.04
EH033_hp@61	pyrite	2377	-548	5.17	0.04
EH033_hp@62	pyrite	2244	-527	5.13	0.04
EH033_hp@63	pyrite	2129	-529	5.14	0.04
EH033_hp@64	pyrite	2016	-559	5.11	0.04

EH033_hp@65	pyrite	1913	-587	4.81	0.04
Son3@22	pyrite standard	3541	1520	1.39	0.04
Son3@23	pyrite standard	3471	1520	1.88	0.04
Son3@24	pyrite standard	3401	1520	1.80	0.04
Son3@25	pyrite standard	3339	1488	1.84	0.04
Son3@26	pyrite standard	-2092	3174	1.44	0.04
Son3@27	pyrite standard	-2158	3205	1.51	0.04
Son3@28	pyrite standard	-2048	3234	1.45	0.04
Son3@29	pyrite standard	-2118	3234	1.54	0.04
Son3@30	pyrite standard	-2188	3234	1.54	0.04
EH033_hp@66	pyrite	2354	-1097	5.37	0.04
EH033_hp@67	pyrite	2179	-1100	5.32	0.04
EH033_hp@68	pyrite	2034	-1098	5.19	0.04
EH033_hp@69	pyrite	2042	-994	5.28	0.04
EH033_hp@70	pyrite	2190	-1012	5.34	0.04
EH033_hp@71	pyrite	2354	-1006	5.44	0.04
EH033_hp@72	pyrite	2401	-872	5.49	0.04
EH033_hp@73	pyrite	2200	-908	5.36	0.04
EH033_hp@74	pyrite	2075	-802	5.29	0.04
EH033_hp@75	pyrite	2257	-831	5.52	0.04
EH033_hp@76	pyrite	2416	-795	5.46	0.04
EH033_hp@77	pyrite	2386	-667	5.46	0.04
EH033_hp@78	pyrite	2171	-745	5.36	0.04
EH033_hp@79	pyrite	2012	-748	5.14	0.04
EH033_hp@80	pyrite	2041	-672	5.13	0.04
EH033_hp@81	pyrite	2119	-607	5.23	0.05
Son3@31	pyrite standard	-2188	3304	1.64	0.04
Son3@32	pyrite standard	-2048	3304	1.54	0.05
Son3@33	pyrite standard	-1978	3374	1.47	0.05
Son3@34	pyrite standard	-2048	3374	1.50	0.05
Son3@35	pyrite standard	-2118	3374	1.62	0.05
Son3@36	pyrite standard	-2082	3432	1.63	0.05